Journal of Nanobiotechnology

RESEARCH

Open Access

Structural optimization of Sr/Zn-phosphate conversion coatings triggered by ions preloading on micro/nanostructured titanium surfaces for bacterial infection control and enhanced osteogenesis

Kangqing Zuo[1,2,3†], Aonan Li[1,2,3†], Taoning Si[2], Weiyi Lei[2], Yusheng Liu[2], Linbo Zhang[2,3], Taixing Zhang[2,3], Guiyong Xiao[4,5*], Yupeng Lu[4,5] and Ningbo Li[1,2,3*]

Abstract

Phosphate conversion coatings on metallic implants can synergistically integrate functional components and structural regulation, offering excellent biocompatibility and osteogenic activity. However, the passive oxide layer on the titanium (Ti) surface impedes the following chemical reactivity, adversely affecting the microstructure and properties of phosphate coatings. This study proposes a strategy for achieving structural optimization and properties enhancement of strontium-zinc phosphate (SrZnP) conversion coatings on Ti via regulating interface chemical reaction between coatings and Ti substrates. The results indicated that Sr^{2+} and Zn^{2+} ions-preloading (IPL) treatment enhanced the interfacial reactivity, which can further achieve crystal refinement and uniform crystal size in nucleation. In contrast, microstructural modifications on Ti substrates induced by acid etching, sandblasting, and alkali etching had minimal effects on the phase composition and crystal morphology (irregular cubic) of the SrZnP coatings. The coatings on IPL-Ti exhibited better mechanical properties and corrosion resistance. Besides, the coatings with optimized structures and surface characteristics elicited bacterial growth inhibition rates of 91.09% and 84.04% against *Staphylococcus aureus* (*S. aureus*) and *Escherichia coli* (*E. coli*), respectively. Meanwhile, the crystal-refined coatings further significantly enhanced the adhesion, proliferation, and differentiation of bone marrow mesenchymal stem cells (BMSCs), proving anticipated osteogenic activity. Overall, the ions preloading strategy on variable micro/nanostructured Ti substrates facilitates the potential application of Sr/Zn-phosphate conversion coatings for repairing infected bone defects.

†Kangqing Zuo and Aonan Li contributed equally to this work.

*Correspondence:
Guiyong Xiao
xiaoguiyong@sdu.edu.cn
Ningbo Li
liningbo@sdfmu.edu.cn

Full list of author information is available at the end of the article

Graphical Abstract

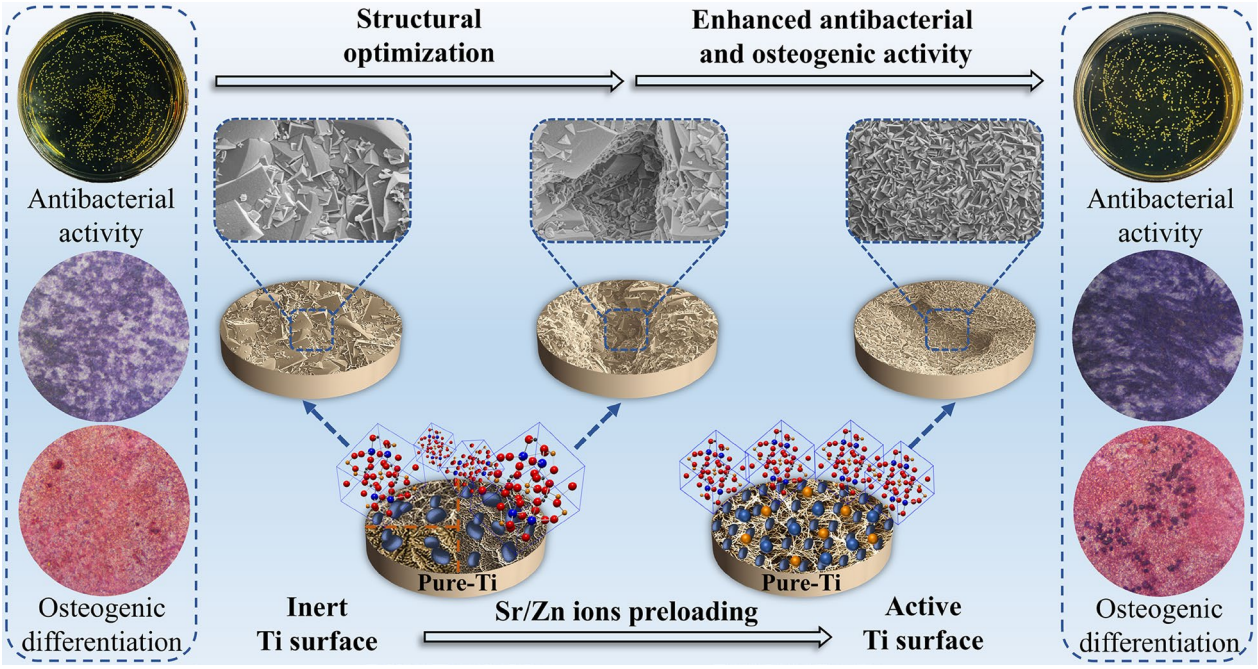

Keywords Ions preloading, Sr/Zn-phosphate conversion coating, Titanium, Interface reaction, Antibacterial capacity, Osteogenic activity

Introduction

Titanium (Ti) and its alloys are commonly used in biomedical applications, including artificial joints, bone repair, cardiovascular stents, and dental implants [1]. However, commercial pure Ti faces surface-related challenges in long-term use, mainly in three areas: (1) Insufficient osseointegration. The mechanical attachment between bioinert pure Ti and bone tissue falls to provide optimal osseointegration [2], limiting the osteoinductive potential of pure Ti implants and increasing the risk of early loosening [3]. (2) Lack of antibacterial activity. The absence of inherent antibacterial properties of pure Ti makes it prone to bacterial biofilm formation [4], which can resist immune responses and hinder antibiotic treatment, increasing infection risk [5]. (3) Corrosion-induced problems. Although pure Ti generally exhibits good biocompatibility, under specific conditions, corrosion products may cause issues, especially due to the joint effect of shear force and body fluid [6]. Corrosion products primarily include Ti oxide particles (e.g., TiO_2 nanoparticles), whose local accumulation may trigger inflammatory responses [7]. Recent studies have shown that orthopedic implants display nanoscale corrosion defects on their surfaces, and nanoparticles can deposit in adjacent muscle tissue, leading to muscle fibrosis proliferation. Transcriptomic analysis revealed that TiO_2 nanoparticles released from the implant surface induce muscle fibrosis by upregulating SNAI2 and activating the PI3K/AKT signaling pathway [8].

To address the aforementioned challenges, surface modification of Ti to enhance its comprehensive performance has become a primary research focus [9]. These surface modification studies enhance the antibacterial and bioactive properties of Ti implants using various physical, chemical, or biological methods. For instance, photocatalytic heterojunction antibacterial coatings, drug-releasing hydroxyapatite coatings, and antibacterial metallic ion-releasing coatings have been constructed [10, 11, 12]. Additionally, the dual antibacterial effect at the microstructure and composition levels has been realized through graphene modification [13]. Moreover, balancing the antibacterial and osteogenic properties is also an important consideration in the design of surface coatings [4]. In recent years, bioactive phosphate coatings have attracted considerable attention in surface modification of metallic implants. Phosphate crystals, consisting of metal cations and phosphate anions, can enable phase composition design based on metal ions and satisfy the biofunctional requirements for metallic implant surfaces. Besides, phosphate crystals exhibit highly versatile morphologies, enabling the incorporation of functional components and the development of micro- and nanoscale

features that support the expression of key biological functions [14]. Currently, phosphate coatings on metallic implant surfaces are primarily designed using elements such as calcium (Ca), magnesium (Mg), zinc (Zn), and strontium (Sr) [15, 16, 17]. Among these, Zn is a vital trace element in bone metabolism that activates key enzymes in osteogenic cells, to promote cell proliferation and differentiation. Zn also enhances collagen synthesis, providing a structural framework for mineral deposition and thereby improving bone strength and density [18]. Furthermore, Zn ions demonstrate significant antibacterial properties, effectively inhibiting the growth of various pathogenic bacteria. The antibacterial mechanism of Zn ions may involve disrupting bacterial cell membranes or interfering with their metabolic pathways, thus impairing normal bacterial metabolic functions and reducing the risk of infection around implants [19]. Sr also exhibits remarkable osteogenic capabilities. Researches indicate that Sr can enhance osteoblast proliferation and differentiation, primarily through the activation of the Wnt/β-catenin signaling pathway, thereby promoting bone formation and increasing bone density. Additionally, Sr can inhibit osteoclast activity by modulating the RANKL/OPG balance, reducing bone resorption, and contributing to bone tissue repair and strengthening [20]. Furthermore, Phosphorus (P) plays a critical role in regulating osteoblast function, promoting their proliferation and differentiation by activating key signaling pathways and regulating osteogenic transcription factors. This directly impacts bone formation, mineralization, and metabolic homeostasis [21, 22]. Additionally, collagen (e.g., type I collagen) and non-collagen proteins (e.g., osteocalcin and osteopontin) in the bone matrix rely on phosphorylation modifications to form a mineralized scaffold [23]. Matrix vesicles secreted by osteoblasts are rich in phosphatases and can hydrolyze pyrophosphate to release free phosphate, initiating the nucleation and growth of hydroxyapatite (HA) crystals [24]. P activates kinases (e.g., FAM20C) to phosphorylate type I collagen, forming a mineralized scaffold that guides HA crystal deposition along collagen fibers [25]. Therefore, zinc-strontium phosphate (SrZnP), a bimetallic phosphate combining Zn and Sr, shows exceptional potential for phosphate coating design. Our preliminary research has demonstrated that SrZnP coatings can promote stem cell osteogenic differentiation and exhibit antibacterial activity. These coatings can induce M2 polarization of macrophages, synergistically enhancing stem cell osteogenic differentiation and highlighting an immunomodulatory osteogenic function [26].

Researchers have developed various techniques for the controlled preparation of phosphate coatings on Ti surfaces, such as biomimetic mineralization [19], micro-arc oxidation [27], plasma electrolytic oxidation [28], spin-coating [29], and hydrothermal treatment [4]. These methods have created functional phosphate coatings on Ti surfaces with multiple phase compositions and microstructural features, achieving improvements in antibacterial and osteogenic properties. Recent research progress has focused on enhancing the biological activity, bonding strength, and functional modifications of these coatings. Phosphate chemical conversion (PCC) is one of the primary methods for fabricating bioactive phosphate coatings on metallic implant surfaces. This technique involves immersing a metal substrate in a phosphating solution, where a chemical reaction forms a dense, insoluble phosphate coating on the metal surface [30]. In addition to its advantages in coating preparation, such as rapid coating formation rate, simplicity, and applicability to irregular substrates, the coatings produced by this technique have excellent corrosion resistance, bioactivity, and strong adhesion to the substrates [14]. Numerous studies have reported the application of PCC in fabricating various phosphate coatings on diverse metallic implant surfaces, such as Mg, Zn, and Ti [16, 31, 32]. In active metals like Mg and Zn, rapid surface corrosion can occur in PCC solutions, disrupting the interfacial microenvironment equilibrium and inducing the deposition and growth of conversion coatings. In contrast, Ti naturally forms a nanoscale oxide passivation layer in oxygen-containing environments, making it chemically inert in PCC solutions. Consequently, conventional PCC treatment faces challenges in forming phosphate coatings on Ti surfaces. Studies suggest that auxiliary techniques are often necessary for PCC treatment on Ti, which can be categorized into four main approaches: (1) conducting chemical conversion in hydrothermal environments under high temperature and pressure [33]; (2) utilizing external energy fields, including ultrasonic, magnetic, current, or electric fields, to enhance conversion coating growth on Ti by providing the required energy [34]; (3) introducing iron (Fe) powder into the PCC solution for maturation treatment, where Fe^{2+} ions act as active centers for crystal nucleation on the Ti surface, facilitating subsequent crystal growth of the conversion coating [35]; and (4) employing electrochemical coupling, wherein a metal with a lower potential than Ti undergoes corrosion to drive the initial chemical conversion, promoting phosphate crystal deposition on the coupled Ti cathode and forming a complete conversion coating [36].

The formation of PCC coatings on Ti surfaces fundamentally involves interfacial interactions between the metal and the solution. To fabricate PCC coatings on Ti, regulating interfacial reactions is crucial to optimize the microstructure and properties of the coatings, as well as improve the bonding quality at the coating-substrate interface. Previous literature has demonstrated that surface activation of metals can be achieved via chemical,

plasma, and mechanical methods, facilitating the successful preparation of conversion coatings on inert metal surfaces [37]. In this study, based on the regulation strategy of interfacial reaction, the Ti substrates were subjected to treatments including sandblasting, acid etching, alkali etching, and ions-preloading, followed by the preparation of SrZnP coatings on various Ti surfaces using the PCC method. The impact of Ti surface pretreatment on the structure and properties of the coatings, including phase composition, microstructure, thickness, roughness, wettability, and corrosion resistance, were systematically investigated. In addition, the evolution mechanisms of the microstructure of the SrZnP coatings regulated by interfacial reactions and the evaluation of antibacterial and osteogenic properties of the coatings were elucidated.

Materials and methods

Coating preparation

Commercial pure Ti (cp-Ti, grade 2) with a diameter of 10 mm and thickness of 3 mm were polished using #400, #600, and #1000 SiC papers, followed by ultrasonic cleaning in acetone, ethanol, and deionized water, and designated as machined-Ti (M-Ti). After that, different pretreatments were applied to the M-Ti disks, as shown in Fig. 1a: (1) The M-Ti disks underwent acid etching in a 4 wt% hydrofluoric acid (HF) solution for 60 s at 25 ℃, and were designated as sanding and acid-etching (SA); (2) According to the process parameters in Table S1, the M-Ti disks were sandblasted and etched in a 4 wt% HF solution for 60 s at 25 ℃, and were designated as sandblasting and acid-etching (SLA); (3) The SLA treated Ti disks were immersed in a 5 M NaOH solution at 60 ℃ for 24 h and were designated as alkali washed after sandblasting and acid-etching (SLAA); (4) The SLAA treated Ti disks were immersed in an ions-preloading solution as per the compositions and process conditions in Table S2, and were designated as ions-preloading (IPL). Finally, the four pretreated Ti disks were ultrasonically cleaned in deionized water for 10 min and stored in ethanol for later use as substrates.

The SrZnP coatings were prepared on the four Ti substrates using a PCC method similar to that described in our previous report [15]. Briefly, the Ti substrates were immersed in a 3 $g{\cdot}L^{-1}$ colloidal titanium phosphate ($Na_4TiO(PO_4)_2{\cdot}(0-7)\ H_2O$) solution at 25 ℃ for 30 s to activate the surface. The pretreated Ti substrates were then incubated in a phosphating solution with pH 3.25 at 70 ℃ for 60 min to execute the coating growth process. The phosphating solution contained 32 $g{\cdot}L^{-1}$ $SrCl_2{\cdot}6H_2O$, 10 $g{\cdot}L^{-1}$ $Zn(H_2PO_4)_2{\cdot}2H_2O$, 14 $g{\cdot}L^{-1}$ $NaH_2PO_4{\cdot}2H_2O$, and 2 $g{\cdot}L^{-1}$ $NaNO_3$. Throughout the process, the chemical reaction was assisted by an external ultrasonic irradiation using an ultrasonic cleaner (40 kHz, 300 W). The coated samples were labeled as C-SA, C-SLA, C-SLAA, and C-IPL, corresponding to their respective substrate pretreatment methods.

Coating characterization

The surface morphologies and elemental compositions of the samples were analyzed using a field emission scanning electron microscope (FE-SEM, Regulus8100, Hitachi, Japan) equipped with an energy-dispersive X-ray spectrometer (EDS). The phase composition was characterized by an X-ray diffractometer (XRD, DMAX-2500PC, Rigaku, Japan) with Cu-Kα radiation (λ = 0.154 nm). The thickness of the coatings was measured using a microprocessor eddy-current thickness gauge (MiniTest 600B, ElektroPhysik, Germany). A Fourier transform infrared spectrometer (FTIR, INVENIO, Bruker, Germany) was used to test functional groups in the 4000–400 cm^{-1} spectral range with a resolution of 4 cm^{-1}. An X-ray photoelectron spectrometer (XPS, Kratos AXIS Supra +, Shimadu, Japan) was used to detect the elemental composition and binding state of the samples. The obtained XPS survey and high-resolution spectra were calibrated with the carbon peak (C 1s, 284.8 eV) and analyzed by the CasaXPS software. The bonding strength of the coatings was evaluated using an electronic universal testing machine (WDW-5, STAR, China) at a tensile rate of 1 $mm{\cdot}min^{-1}$, following the ASTM C633 – 01 standard. Before testing, the samples (Φ10 × 3 mm) were bonded to stainless-steel cylinders using an acrylic adhesive and cured at room temperature for 24 h. Five replicates were tested per sample group, with the bonding strength calculated as the average of three consistent measurements. The surface roughness of the samples was assessed using a laser scanning confocal microscope (LSCM, LSM-800, Zeiss, Germany). The surface wettability of the coatings was determined at room temperature using a contact angle goniometer (DSA100S, KRUSS, Germany) based on the sessile drop method. The static contact angle (θ) was measured by dropping 2 μL of deionized water on the surface and recording the θ values after 30 s. The measurement was repeated five times to ensure stable results. The ions release was evaluated in triplicate by immersing the coated samples in 10 mL physiological saline solution (0.9 wt% NaCl aqueous solutions) at 37 °C for 0.5, 1, 4, 7, and 14 days. At each time point, 1 mL of the immersed solution was taken out for testing, and the same volume of fresh solution was added. The cumulative amounts of released ions (Sr, Zn, and P) were measured by an inductively coupled plasma optical emission spectrometer (ICP-OES 730, Agilent, Japan).

Electrochemical measurements

The corrosion resistance of the coatings, including open circuit potential (OCP), potentiodynamic polarization

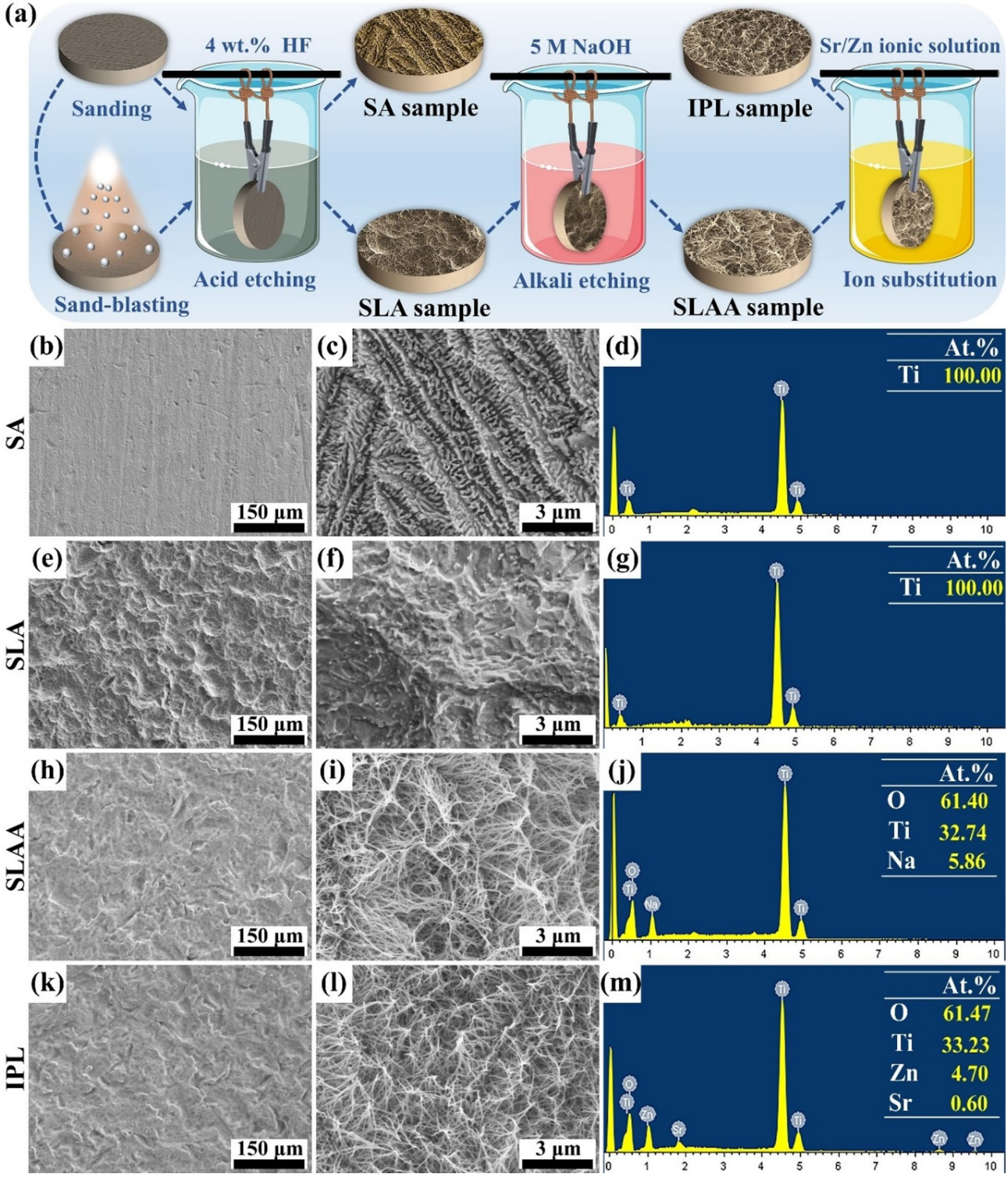

Fig. 1 (**a**) Schematic illustration of pretreatment processes applied to Ti substrates. FE-SEM images and corresponding elemental compositions of Ti substrates under different pretreatment conditions: (**b**–**d**) SA, (**e**–**g**) SLA, (**h**–**j**) SLAA, and (**k**–**m**) IPL

(PDP), and electrochemical impedance spectroscopy (EIS), was experimented in simulated body fluid (SBF) at 37 °C using an electrochemical workstation (CHI660e, China). The tests were performed in a standard three-electrode cell, including a saturated calomel electrode (SCE), a platinum (Pt) sheet, and the sample as the reference electrode, counter electrode, and working electrode, respectively. After a stabilization period of

1800 s for OCP measurements, EIS tests were executed with the sinusoidal perturbing signal of 5 mV and the frequency range from 10^5 Hz to 10^{-2} Hz. The obtained EIS data were fitted and analyzed by the Zview software. The PDP tests were conducted at a scan rate of 1 $mV{\cdot}s^{-1}$ over a potential range of − 0.5 V to + 0.5 V vs. OCP. The corrosion potential (E_{corr}) and corrosion current density (I_{corr}) were determined from the PDP curves via the Tafel-type linear extrapolation method.

In vitro antibacterial tests

Bacterial culture and morphology

Gram-positive *Staphylococcus aureus* (*S. aureus*, ATCC 25923) and Gram-negative *Escherichia coli* (*E. coli*, ATCC 25922) were used to evaluate the bacterial growth inhibition property of the samples. The bacteria were cultured in sterile Luria-Bertani (LB) broth and agar plates, prepared using standard procedure. After growing in LB broth at 120 rpm and 37 °C for 16 h, the bacterial suspensions were diluted to an optical density at 600 nm (OD600) of 0.30 for use in the experiments.

To examine bacterial adhesion and morphology on the sample surfaces, 100 μL of bacterial suspensions were seeded onto the samples and incubated at 37 °C for 24 h. Following incubation, the samples were gently rinsed with phosphate-buffered saline (PBS) and fixed with 4% paraformaldehyde (PFA) at 4 °C for 30 min. Then sequentially dehydrated using ethanol gradients (30%, 50%, 70%, 95%, and 100% v/v), with each step lasting for 10 min. After dehydration, the samples were sputter-coated with gold and observed using FE-SEM.

Antibacterial rates

After 24 h of incubation, the adhered bacteria on the sample surfaces were suspended in 2 mL of PBS by ultrasonic vibration (40 kHz, 300 W) for 10 min, followed by vortex mixing for 2 min. The resulting bacterial suspensions were serially diluted (10^6-fold), and 100 μL of each dilution was spread onto LB agar plates. The plates were incubated at 37 °C for 24 h, after which images of the LB plates were captured, and the number of bacterial colonies was counted. The antibacterial rates of each sample were calculated using the following equation:

Antibacterial rate (%) = $(N_{control} - N_{sample}) / N_{control} \times 100\%$,

where $N_{control}$ and N_{sample} denote the number of bacterial colonies in the M-Ti group and the coated Ti group, respectively.

Cell culture

Rat-derived bone marrow mesenchymal stem cells (BMSCs; Pricella, China) were cultured in growth medium (GM), which consisted of Dulbecco's modified Eagle's medium (DMEM; Gibco, USA) supplemented with 10% fetal bovine serum (FBS; Saiye, China) and 1% penicillin-streptomycin (Solarbio, China). For osteogenic differentiation, BMSCs were maintained in osteogenic differentiation medium (OM) prepared by supplementing GM with dexamethasone (1×10^{-8} mol/L; Sangon, China), β-glycerophosphate disodium salt hydrate (1×10^{-2} mol/L; Solarbio, China), and ascorbic acid (50 μg/mL; Solarbio, China). All cultures were incubated at 37 °C in a humidified atmosphere containing 5% CO_2.

Cell adhesion and proliferation

The BMSCs (1×10^4 cells/well) were seeded on the sample surfaces in 24-well plates. After 24 h of culture, the samples were gently rinsed with PBS and fixed with 2.5% glutaraldehyde at 4°C for 4 h. They were then dehydrated using a graded ethanol series (30%, 50%, 70%, 80%, 90%, and 100% v/v). Finally, the cell morphologies were observed using FE-SEM after drying and sputter-coating with gold.

The structure of the cell cytoskeleton was observed using F-actin staining. BMSCs (1×10^4 cells/well) were incubated on the samples for 24 h, followed by fixing with 4% PFA for 30 min. Then the rhodamine-phalloidin (Solarbio, China) and 4,6-diamidino-2-phenylindole (DAPI; Solarbio, China) were used to stain the nuclei and actin filaments, respectively. The stained cytoskeletal structures were visualized using the LSCM (LSM 900, Zeiss, Germany).

The cell viability of the samples was evaluated using a Live/Dead assay. BMSCs were seeded onto the sample surfaces at a density of 1×10^4 cells/well and incubated for 48 h. Subsequently, a Live/Dead staining kit (Solarbio, China) containing Calcein acetoxymethyl ester (Calcein-AM) and Propidium iodide (PI) was used to stain cells for 30 min at 37 °C. The live cells (green fluorescence) were visualized using fluorescence microscopy (ICX41, SOPTOP, China). The number of live cells on the samples was quantified using Image J.

BMSCs (1×10^4 cells/well) were seeded onto the samples in 24-well plates and incubated for 1, 3, and 5 days. At each time point, 10% (v/v) Cell Counting Kit-8 (CCK-8; Biosharp, China) solution was added to each well and incubated for 2 h. After incubation, 100 μL of the supernatant was transferred to 96-well plates, and the absorbance at 450 nm was measured using a microplate reader (TECAN SPARK, Switzerland).

Osteogenic differentiation

Alkaline phosphatase (ALP) staining

After 14 days of culture, ALP staining was conducted using a BCIP/NBT ALP Color Development Kit (Beyotime, China). The BMSCs were fixed with 4% PFA and stained with the staining solution for 1 h, followed by

observation under a microscope (Nikon LV100ND, Japan). Meanwhile, the BMSCs were lysed and incubated with an ALP assay kit for 30 min to quantify the ALP activity at 520 nm using a microplate reader.

Alizarin red S (ARS) staining

After 14 days of culture, the cells were fixed with 4% PFA and stained with 1% ARS solution (Solarbio, China). The staining patterns were observed under an inverted microscope (Nikon LV100ND, Japan). For quantitative analysis, the bound ARS stain was dissolved using 10% cetylpyridinium chloride (Aladdin, USA), and the OD value was measured at 570 nm.

Immunofluorescence (IF) staining

At 7 and 14 days, the cells were fixed in 4% PFA and permeated in 0.1% Triton X-100 solution, osteopontin (OPN) and runt-related transcription factor-2 (Runx2) primary antibodies were added to the wells, and incubated overnight at 4 °C. Then, the primary antibodies were washed and incubated with Alexa Fluor 594-labeled secondary antibodies for 2 h. The cell nuclei were stained with DAPI. The fluorescent cellular images were captured using LSCM.

Real-time polymerase chain reaction (RT-PCR)

Four replicate samples from each group were placed in a 6-well culture plate. Cell suspensions with a density of 20×10^4 per well were seeded onto the sample surfaces. The next day, the medium was replaced with OM. After 7 and 14 days of osteogenic induction, total RNA was extracted using the SteadyPure Universal RNA Extraction Kit II (Accurate Biology, China). The extracted RNA was reverse-transcribed into complementary DNA (cDNA) using the Evo M-MLV RT Premix (Accurate Biology, China). Real-time quantitative PCR (RT-PCR) was performed using the SYBR® Green Premix Pro Taq HS qPCR Kit (Accurate Biology, China). The relative gene expressions of ALP, collagen type I (Col-I), and osteocalcin (OCN) were normalized to glyceraldehyde 3-phosphate dehydrogenase (GAPDH) and calculated using the $2^{-\Delta\Delta Ct}$ method ($n = 4$). The primer sequences utilized are listed in Table S3.

Statistical analysis

All results were shown as the mean ± standard deviation (SD) from at least three replicates. Statistical significance among different groups was evaluated using an independent sample t-test in GraphPad Prism 8 software. Symbols *, #, △, and ◇ indicate $P < 0.05$, **, while ##, △△, and ◇◇ represent $P < 0.01$, and ***, ###, △△△, and ◇◇◇ indicate $P < 0.001$, corresponding to comparisons with M-Ti, C-SA, C-SLA, and C-SLAA, respectively.

Results and discussion

Microstructure and phase compositions

The FE-SEM images of the Ti substrate surface under the four pretreatment conditions are shown in Fig. 1b–m. As depicted, the SA sample exhibits a relatively smooth and flat surface with sporadically distributed etching pits caused by HF corrosion, presenting a submicron ridge-like and serrated microstructure (Fig. 1b, c). The SLA sample displays a significantly roughened surface with a dual structure. The craters formed by sand impacts range from 5 to 30 μm in diameter, while their inner walls are etched by HF, resulting in a submicron sharp serrated morphology (Fig. 1e, f). The SLAA sample maintains the roughened surface formed by sandblasting, while the degree of roughness is weakened as some of the small-diameter sandblasted craters have disappeared. In addition, the micro-nano porous structure resulting from the reaction between Ti and NaOH is evident on the surface of the SLAA sample, consistent with the typical morphology of a sodium titanate ($NaTiO_3$) gel layer (Fig. 1h, i) [38]. In contrast, the ions-preloading treatment does not significantly affect the microstructure of the samples, as the IPL sample retains the same surface morphology characteristics as the SLAA sample (Fig. 1k, l).

The corresponding EDS results reveal that the SA and SLA treatments do not alter the elemental composition of the Ti substrate. In contrast, the SLAA sample surface shows a higher content of O (61.40 at%) and Na (5.86 at%) due to NaOH corrosion. Comparatively, the IPL sample surface contains Zn and Sr elements but no detectable Na, indicating that Zn^{2+} and Sr^{2+} ions can replace Na^+ during the IPL treatment. Despite the 10:1 molar concentration ratio of Sr^{2+} to Zn^{2+} in the ions-preloading solution (Table S2), the Zn content on the IPL sample surface (4.70 at%) is much higher than that of Sr (0.60 at%). This suggests that Zn^{2+} preferentially replaces Na^+ in the porous layer of the SLAA sample. This may be due to the difference in ionic radii. The radius of Zn^{2+} (0.74 Å) is smaller than that of Sr^{2+} (1.13 Å) [39, 40], making Zn^{2+} more easily exchangeable with Na^+ in $NaTiO_3$. Similar results have been reported in the previous research [19].

The four pretreated Ti substrates were immersed in the phosphating solution for chemical conversion treatment, and the resulting morphologies and elemental compositions of the coatings are presented in Fig. 2. The overall surface roughness of the conversion coatings corresponds closely to that of the underlying Ti substrates. Among the samples, the C-SA surface is the smoothest, while the C-SLA, C-SLAA, and C-IPL surfaces retain the roughened characteristics imparted by sandblasting. At the microstructure level, all four coatings consist of tightly packed cubic crystals. The C-SA, C-SLA, and C-SLAA samples exhibit crystals of varying sizes, whereas the C-IPL sample features much finer, uniformly

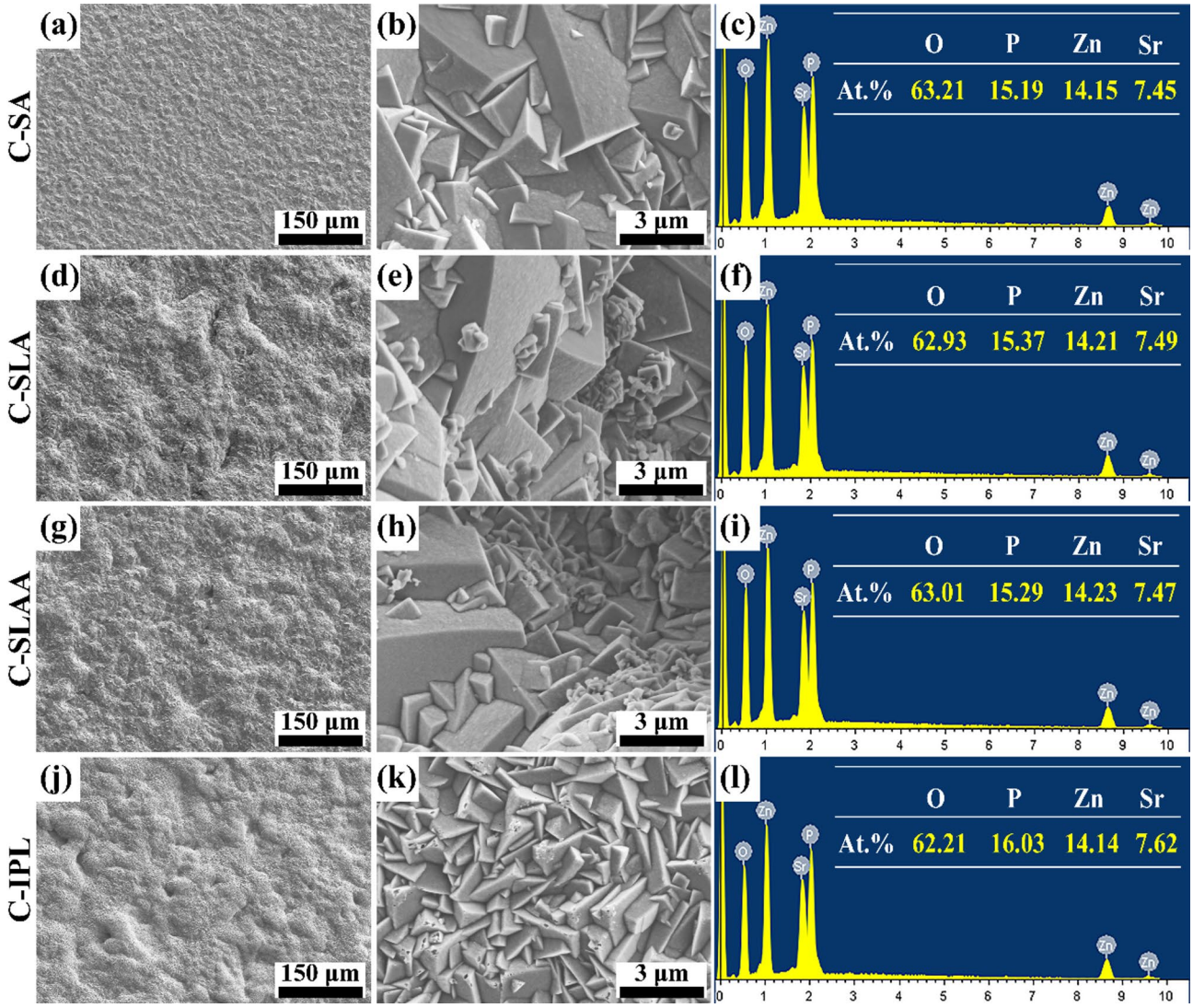

Fig. 2 FE-SEM images and corresponding elemental compositions of the SrZnP coatings on Ti substrates under different pretreatment conditions: (**a**–**c**) C-SA, (**d**–**f**) C-SLA, (**g**–**i**) C-SLAA, (**j**–**l**) C-IPL

sized crystals. This observation suggests that the ions-preloading treatment enhances the surface activity of the Ti substrate, promoting nucleation and leading to crystal refinement. Additionally, the EDS spectra reveal that all four coatings contain the elements O, P, Zn, and Sr. The relative contents of these elements are consistent across the coatings, suggesting that the different pretreatment states of the Ti surface have minimal impact on the elemental composition of the phosphate coatings. These findings indicate that the crystal formation of the coatings is not particularly sensitive to the surface roughness or micro-nano structures of the Ti substrate. Instead, the chemical composition of the substrate surface plays a more significant role in determining the crystal size. Specifically, the preloading of the coating component ions can reduce the size and improve the homogenization of the crystals.

The XRD patterns of SA, SLA, SLAA, and IPL substrates, along with the phosphate coatings on their surfaces, are shown in Fig. 3a **and b**. The diffraction peaks of the bare Ti substrates under all four pretreatment conditions are consistent with the Ti standard PDF card (JCPDS #44-1294). An increase in (100) crystalline diffraction intensity and a decrease in (102) and (103) crystalline diffraction intensities in SLA, SLAA, and IPL substrates, compared to SA, is attributed to surface roughening caused by sandblasting. Furthermore, the XRD peaks of the porous gel layer of sodium titanate are absent on the surface of SLAA and IPL substrates, potentially due to a thinner porous layer and lower crystallinity. The coatings on the surfaces of all four Ti substrates exhibit similar XRD diffraction peaks, which are indexed to the strontium-zinc-phosphate ($SrZn_2(PO_4)_2$, JCPDS #50–0159) phase. In addition, the FTIR spectra

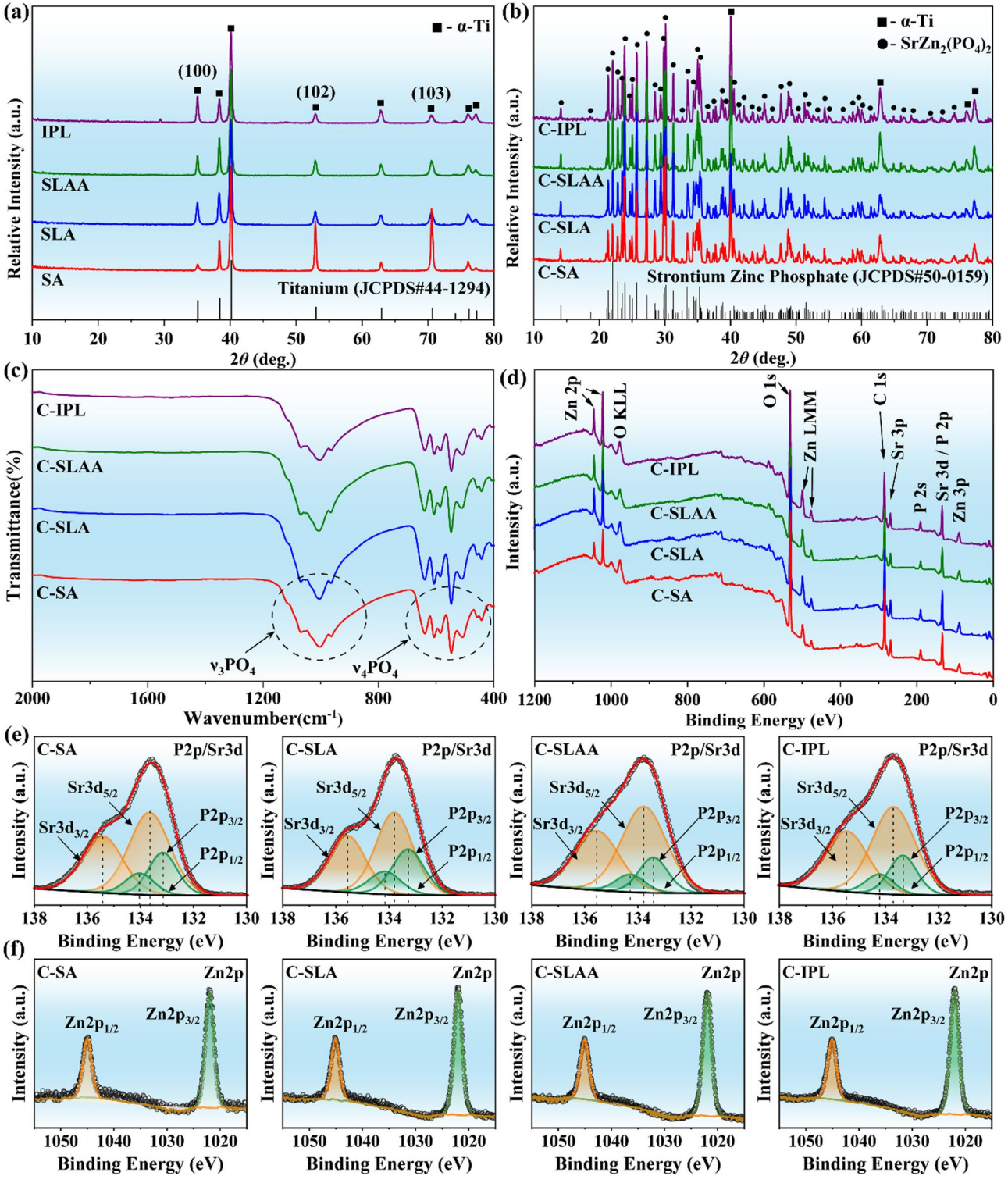

Fig. 3 XRD patterns of Ti substrates before (**a**) and after (**b**) being coated with SrZnP coatings under various pretreatment conditions. (**c**) FTIR spectra of the coated samples. (**d**) Survey scanning spectra, and high-resolution spectra of (**e**) P2p/Sr3d and (**f**) Zn2p of the coated samples

of all coated samples exhibit typical absorption peaks of PO_4^{3-} (Fig. 3c). Specifically, the peaks between 400 and 700 cm^{-1} correspond to O–P–O bending mode, and the peaks between 900 and 1200 cm^{-1} pertain to the P–O stretching vibration mode of PO_4^{3-}. The XPS survey spectra (Fig. 3d) further confirm the O, P, Zn, and Sr elemental compositions of the four coated samples. As shown in Fig. 3e, the spectra of Sr3d and P2p show overlaps in the

high-resolution peaks, which can be separated into two distinct doublets. The doublets of Sr3d consist of $Sr3d_{3/2}$ and $Sr3d_{5/2}$ peaks with the correct relative intensity ratio (2:3) and the spin-orbit energy around 1.8 eV. Similarly, the P2p doublets also consist of two split peaks of $P2p_{1/2}$ and $P2p_{3/2}$, with a relative intensity ratio of about 1:2 and a separation energy of around 0.8 eV. Figure 3f shows the spectra of Zn2p, containing two peaks of $Zn2p_{1/2}$ and $Zn2p_{3/2}$ with the separation energy around 23.1 eV. All these results suggest that the pretreatment state of the substrate has little effect on the crystalline phases of the SrZnP phosphate coatings.

The findings suggest that the key to inducing microstructural evolution in phosphate coatings on Ti surfaces via interface reaction regulation lies in the surface composition of titanium, specifically the preloaded metallic ions for coating formation, rather than its micro/nanostructures. Figure 4 presents a schematic illustrating the structural evolution of SrZnP conversion coatings on titanium surfaces, driven by interface reaction regulation. As shown, after SA, SLA, and SLAA treatments, the Ti substrate surfaces develop rough, jagged, and porous micro/nanostructures. However, these structural changes do not alter the inert nature of the Ti surface during the chemical reaction process, meaning the surface does not undergo corrosion to provide the initial driving force for phosphate coating growth. Instead, the growth of the SrZnP coating relies on supersaturation of the phosphating solution at the Ti-solution interface, induced by ultrasonic agitation. The ionic composition of the coating is entirely derived from the phosphating solution. The inert Ti surface induces uneven nucleation, leading to significant crystal size variations within the coating. In contrast, the IPL-treated Ti surface contains preloaded Sr^{2+} and Zn^{2+} ions, which are actively released during the coating formation process, promoting supersaturated deposition of $SrZn_2(PO_4)_2$ crystals at the Ti-solution interface. This chemical reactivity results in an active Ti surface that induces uniform nucleation and increases the number of nucleation sites. With more nucleation points, the induction period for coating formation is shortened, and the initial number of nuclei increases. The limited space for crystal growth leads to smaller and more uniform crystal sizes in the obtained coating.

Zhang et al. [37] found that sandblasting stainless steel substrates significantly reduced the crystal size of Hopeite phosphate coatings. In addition, Turk et al. [41] found that NaOH pretreatment of Ti improved the nucleation

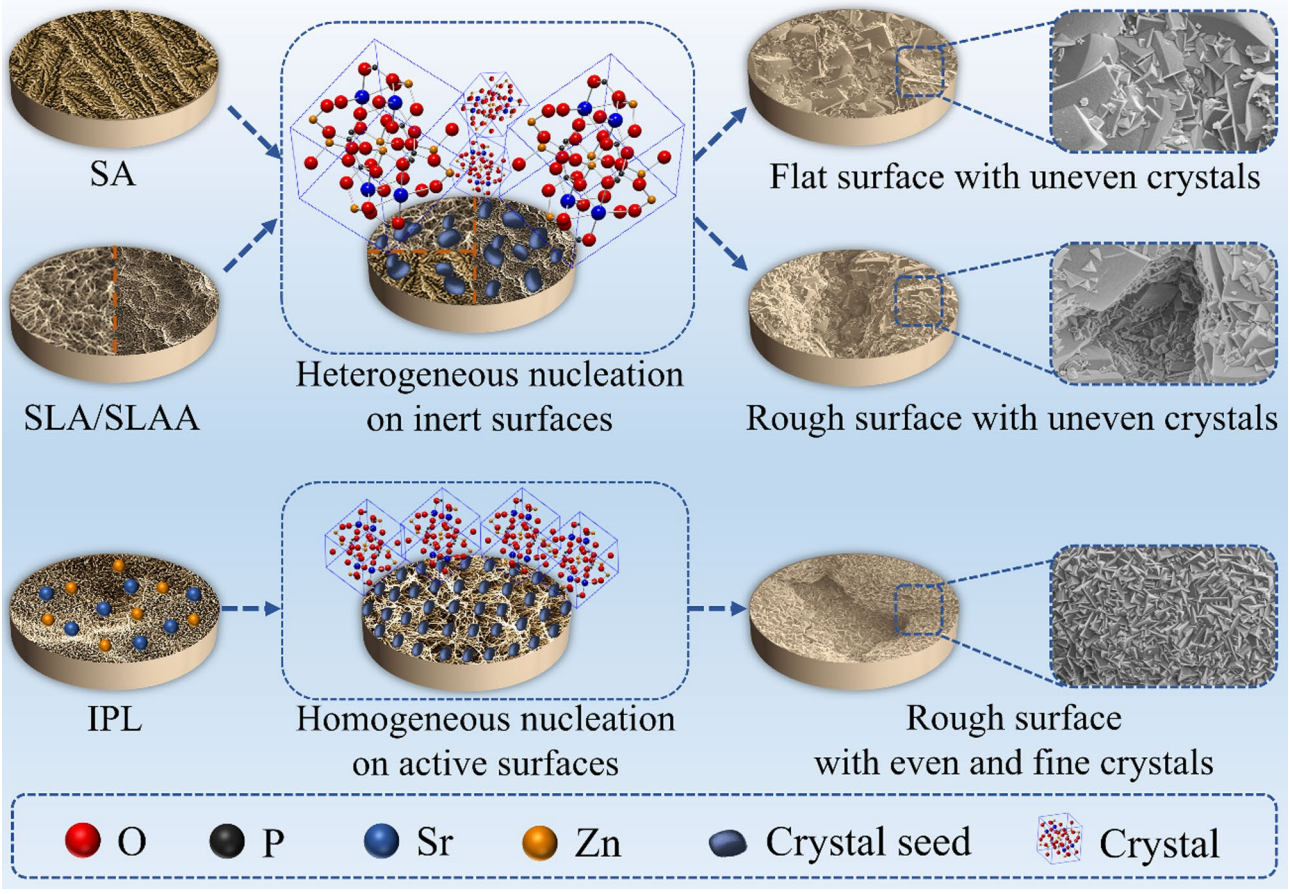

Fig. 4 Schematic illustration of the structural evolution of SrZnP conversion coatings on Ti induced by regulating interface reactions

uniformity of biomimetic HA coatings. In contrast, the grain size and morphology of the SrZnP coatings on the SLA and SLAA substrates in this study did not change significantly compared to the SA substrate. This phenomenon is related to the chemical inertness of the Ti substrate in the phosphating solution, and the change in its surface physical properties did not significantly affect the nucleation growth of phosphate crystals. Furthermore, the Na^+ on the surface of SLAA does not participate in coating formation. Wang et al. [19] placed Sr^{2+} and Zn^{2+} on the Ti surface through alkali heat and ionic substitution, followed by biomimetic deposition to prepare coatings with uniform crystal size. Similarly, the preloading of Sr^{2+} and Zn^{2+} in this study can enhance the chemical activity of the Ti substrate in the reaction. Moreover, the micro- and nanoporous mesh structure provides a large contact area with the phosphating solution, and the released Sr^{2+} and Zn^{2+} can increase the interfacial supersaturation, promoting uniform nucleation deposition of phosphate crystals.

Coating thickness and bonding strength

The cross-sectional morphologies of the C-SA, C-SLA, C-SLAA, and C-IPL samples are shown in Fig. 5a. The results indicate that the coatings exhibit an internally dense monolayer structure, are well bonded to the Ti substrates, and have crystal particles fused as a whole. The surface topography of the coatings is characterized by the exposed edges of the surface crystals. In addition, the coatings on the SA sample exhibit flat cross-sections and uniform thicknesses, while the coatings on the SLA, SLAA, and IPL samples reveal vertical undulations that follow the rough morphology of the substrate after sandblasting. Notably, different areas of the coatings show consistent thicknesses. This result indicates that the Ti substrate surface pretreatment, including sandblasting, acid etching, alkaline etching, and ions-preloading, did not significantly affect the internal structure of the SrZnP conversion coating or the interfacial bonding properties of the coating-substrate. This is because the growth of SrZnP coatings, particularly their phase composition and crystal morphology, is controlled by the microenvironment of the phosphating solution adjacent to the Ti substrate. The consistency of this microenvironment ensures stability in the phase composition and crystal morphology. Moreover, the cubic $SrZn_2(PO_4)_2$ crystals, which are micrometer-sized, are insensitive to the micro- and nano-scale morphology formed by acid and alkali etching.

To compare the effects of different Ti substrate pretreatments on the thickness of SrZnP coatings, the samples obtained under the four conditions were quantitatively examined using a thickness gauge, with results shown in Fig. 5b. The C-SA sample exhibits the greatest

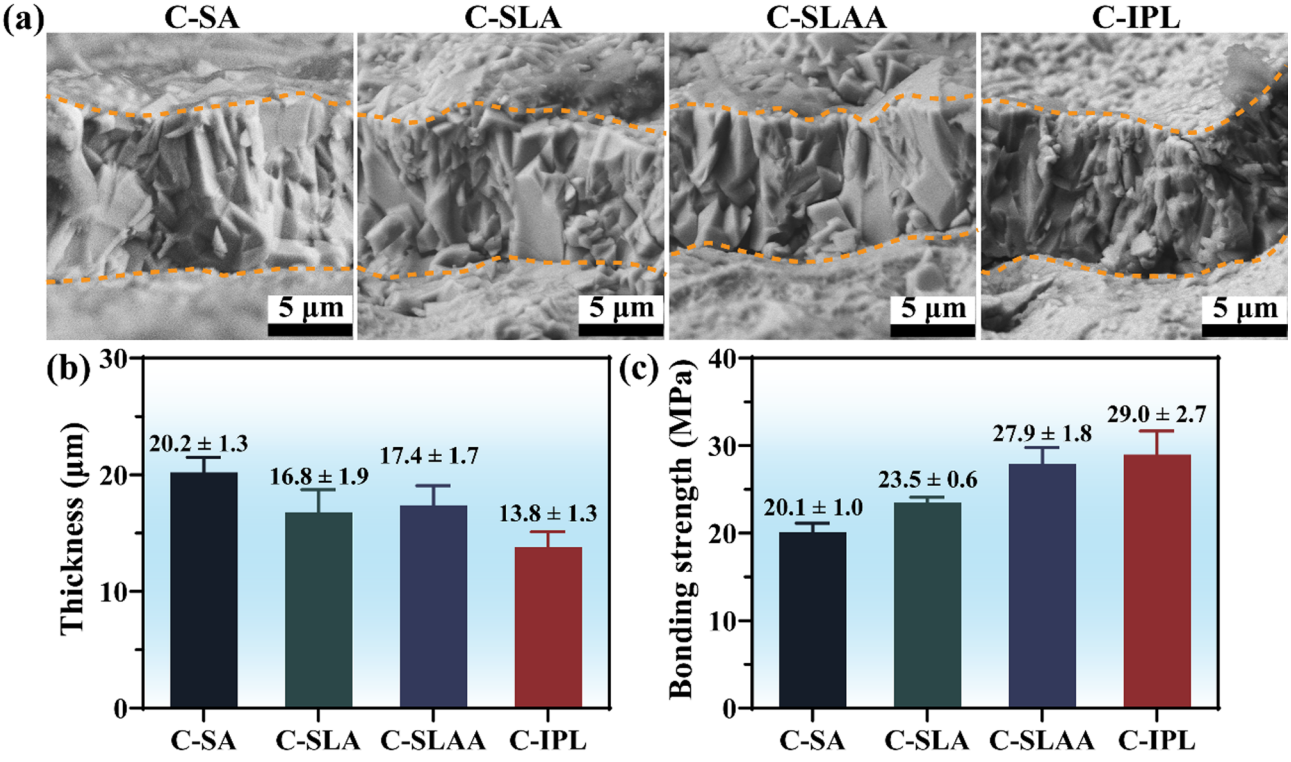

Fig. 5 (**a**) FE-SEM cross-sectional images, (**b**) thickness, and (**c**) bonding strength of SrZnP coatings on Ti substrates under different pretreatment conditions ($n = 3$)

thickness, approximately 20 μm. The coating thickness of the SLA sample is approximately 17 μm, indicating that sandblasting reduces the coating thickness. This reduction is likely due to the rough surface produced by sandblasting, which generates more active nucleation points. The coating thickness of the C-SLAA sample is similar to that of the C-SLA sample, suggesting that the sodium titanate gel layer formed by alkali etching and its micro/nano-porous structure have no significant effect on coating thickness. In contrast, the coating thickness of the C-IPL samples is reduced to approximately 14 μm, consistent with the fine and uniform grain size. The thickness of the conversion coating affects its bonding strength and, consequently, its structural stability. Figure 5c illustrates the bonding strength of SrZnP coatings on Ti substrate under four pretreatment conditions. The bonding strength of the coatings ranges from 20 to 30 MPa, and its variation is inversely correlated with the coating thickness. This suggests that surface roughening of the substrate and reduced coating thickness can enhance bonding strength. In addition, the bonding strength of the C-SLA sample is comparable to that of Hopeite coatings on sandblasted stainless steel surfaces (21.19 ± 2.90 MPa) [37]. However, the bonding strength of the C-SLAA and C-IPL samples is lower than that of the coatings obtained through biomimetic deposition on similar pretreated Ti surfaces (35–40 MPa) [19]. This discrepancy may arise because the SrZnP coatings are thicker than the biomimetic deposition coatings (approximately 5 μm).

The results indicate that the bonding strength of the PCC coating is strongly influenced by the surface state of the Ti substrate. The bonding strength of SrZnP conversion coatings can be enhanced through sandblasting, acid etching, alkali etching, and ions-preloading treatment on the Ti substrate surface. This improvement can be attributed to three factors. First, the surface roughness created by sandblasting increases the contact area between the coating and the substrate, enhancing the anchoring and interlocking effects between the coating and the substrate surface. Second, the micro/nano-scale porous layered structure generated by alkali etching serves as a transition layer, enhancing the bonding strength between the PCC coating and the Ti substrate. Thirdly, the preloading of Sr^{2+} and Zn^{2+} transforms the Ti surface from inert to active in the phosphating solution. The released Sr^{2+} and Zn^{2+} on the surface promote the interfacial coating formation reaction, shortening nucleation time, increasing nucleation rate, and significantly reducing crystal size and coating thickness, thereby enhancing bonding strength. Thus, appropriate pretreatment of the Ti substrate can enhance its surface quality in terms of morphology and composition, ultimately improving the bonding performance of the PCC coating.

Surface roughness and wettability

LSCM was employed to further characterize the surface topography of the coatings on different Ti substrates, as shown in Fig. 6a. The M-Ti surface exhibits parallel scratches and a relatively smooth appearance with minimal irregularities. After PCC treatment, all four coated samples display irregular peaks (red) and valleys (blue), attributed to phosphate crystal growth. The C-SA sample exhibits a relatively smooth appearance, while the C-SLA, C-SLAA, and C-IPL samples demonstrate more undulating topographies, corresponding to hill-like crests and etch pits on the substrates. These images reveal the characteristic topographies for the samples, consistent with the SEM analysis (Fig. 2). Figure 6b presents the quantitative surface average roughness (Sa) based on the LSCM images. Compared to C-SA (0.71 μm), the roughness of the C-SLA, C-SLAA, and C-IPL samples significantly increased, attributed to the surface roughening of the substrate caused by sandblasting. The C-SLA sample exhibits the highest Sa value (3.19 μm), while the C-SLAA sample shows a lower Sa of 2.83 μm, correlating with the reduction in substrate surface roughness caused by alkali etching. Additionally, the roughness of the C-IPL sample decreases to 2.39 μm, likely due to its finer and more uniformly sized crystals.

The microstructure formed on the Ti implant surface after SLA treatment enhances surface roughness, facilitating mechanical interlocking and biomechanical stability, thereby improving osseointegration [42]. In this study, the SrZnP coating modified the microstructural characteristics of the pretreated Ti substrates, including the spike-like nanofeatures on SLA surfaces and the porous structures on SLAA and IPL surfaces. However, in terms of roughness, the SrZnP coating has minimal impact on the initial roughness values of the substrates. The roughness (Sa) measurements of the four substrates (SA, SLA, SLAA, and IPL) are presented in Fig. S1. A comparison of Fig. 6b and Fig. S1 indicates that the C-SLA, C-SLAA, and C-IPL samples exhibit Sa values comparable to their respective substrates. Additional roughness parameters, including root mean squared roughness (Sq) and peak-valley roughness (Sz), further support this observation (Fig. S2). Although $SrZn_2(PO_4)_2$ crystals within the SrZnP coating exhibit relatively regular morphologies and smooth surfaces, their stacking and interlocking contribute to a roughened coating surface. Notably, the C-IPL sample maintains a roughness comparable to that of the SLA substrate, while the refinement of its grain structure increases the effective surface area, potentially enhancing mechanical interlocking and biomechanical stability by improving bone contact. Furthermore, the SrZnP coating demonstrates a synergistic effect between its microstructural features and functional composition, reinforcing osseointegration by inhibiting bacterial

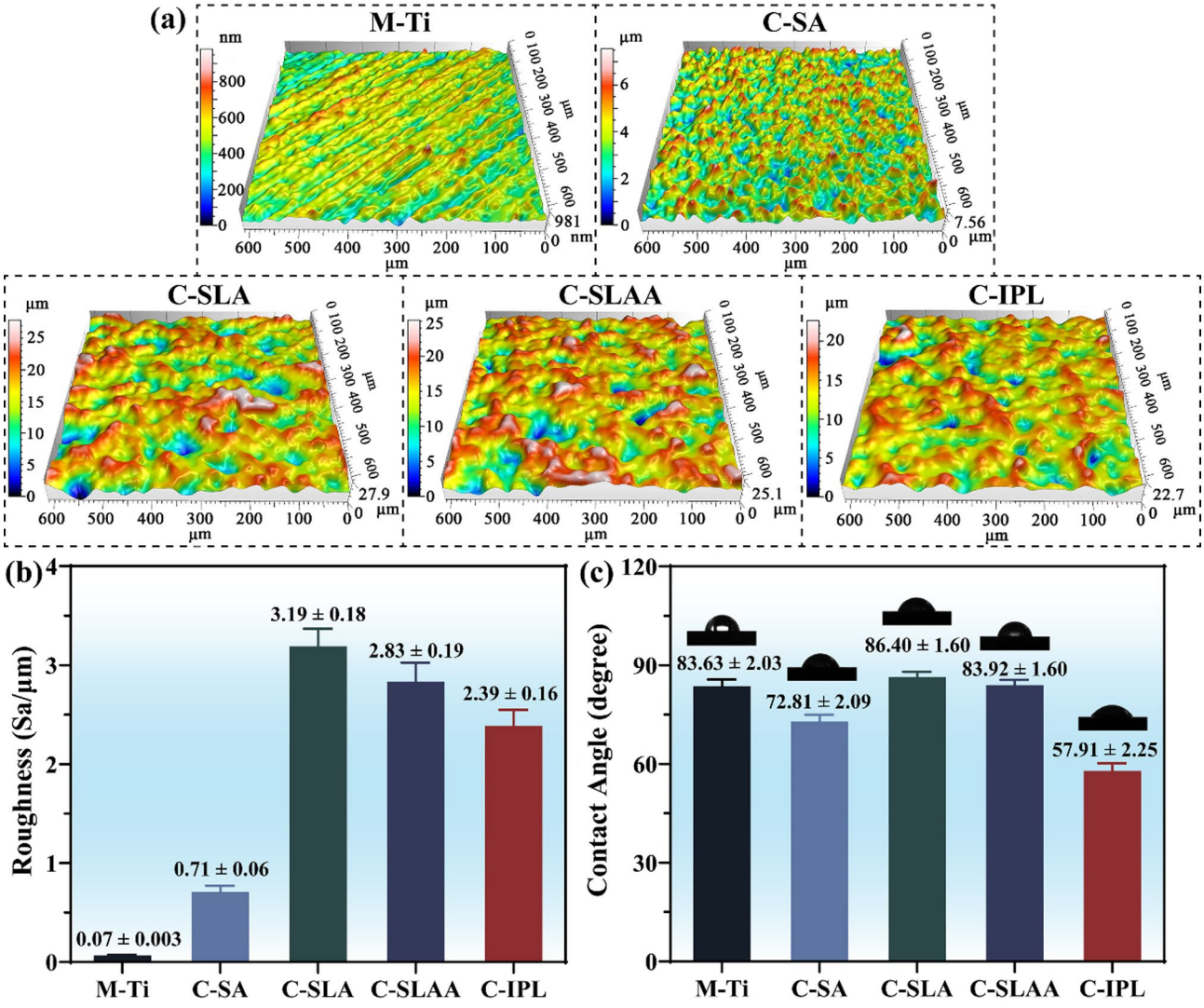

Fig. 6 (**a**) 3D topographical images from LSCM, (**b**) quantitative surface roughness measurements, and (**c**) contact angles of SrZnP coatings on Ti substrates under different pretreatment conditions ($n = 3$)

infection, promoting biomineralization, and enhancing cellular responses, thereby compensating for the limitations of mechanical interlocking [15].

Digital images of water droplets and their corresponding contact angles on M-Ti and the four coated samples are presented in Fig. 6c. Compared to M-Ti (83.63 ± 2.03°), the contact angle decreases to 72.81 ± 2.09° for the C-SA sample, indicating the enhancement of the coating on Ti substrate hydrophilicity. The C-SLA sample shows the largest contact angle (86.40 ± 1.60°) among the coated samples. In line with reduced roughness, the contact angles of C-SLAA and C-IPL samples decrease to 83.92 ± 1.60° and 57.91 ± 2.25°, respectively. Moreover, the hydrophilicity of the C-IPL sample surpasses that of C-SA, suggesting that a uniform surface structure and fine crystal size offset surface roughening effects and significantly enhance hydrophilicity. The wettability of the coating surface is influenced by various factors, including chemical composition, roughness, and microstructure. The contact angle of the C-SA sample is approximately 72°, demonstrating the hydrophilic properties of $SrZn_2(PO_4)_2$ crystals. In comparison to C-SA, the contact angles of C-SLA and C-SLAA are higher, which can be explained by the Cassie-Baxter model [43]. This model suggests that the pit structure of rough surfaces may trap air when a droplet falls, creating an air cushion that hinders the contact between the droplet and the hydrophilic $SrZn_2(PO_4)_2$ crystals. Despite the roughened surface of C-IPL, its crystal size is significantly reduced in the microstructure and is more uniform, with a larger specific surface area. These microstructural features can weaken the formation of an air cushion between the rough surface and the droplet, promoting a greater contact area between the $SrZn_2(PO_4)_2$ crystals

and the droplet, thus encouraging the droplet to spread and exhibit good hydrophilicity.

Electrochemical corrosion behaviors

Electrochemical tests were conducted on M-Ti and the four coated samples to evaluate their corrosion behaviors. A passive oxide layer, primarily composed of TiO_2, exists on the surface of M-Ti, providing good corrosion resistance in SBF. Comparing the electrochemical behavior of the coated samples with that of M-Ti allows for a clear analysis of their corrosion resistance. Figure 7a presents the PDP curves of all samples. The M-Ti sample exhibits a typical corrosion damage process of its oxide layer in the anodic region of the PDP curve. Similar PDP curves, lacking an obvious passive region, are observed in all coated samples. Table 1 summarizes the calculated electrochemical parameters derived from the PDP curves, including corrosion potential (E_{corr}), corrosion current density (I_{corr}), anode slope (β_a), cathode slope (β_c), and polarization resistance (R_p, calculated as $R_p = (\beta_a \cdot |\beta_c|) / (2.303 \cdot I_{corr} \cdot (\beta_a + |\beta_c|))$) [44]. Although the E_{corr} values of the coated samples are similar to or slightly more negative than that of M-Ti, all four coated samples exhibit lower I_{corr} and higher R_p, indicating enhanced anti-corrosion properties. Furthermore, compared to C-SA, the I_{corr} of C-SLA, C-SLAA, and C-IPL samples decreases, while their R_p increases approximately twofold.

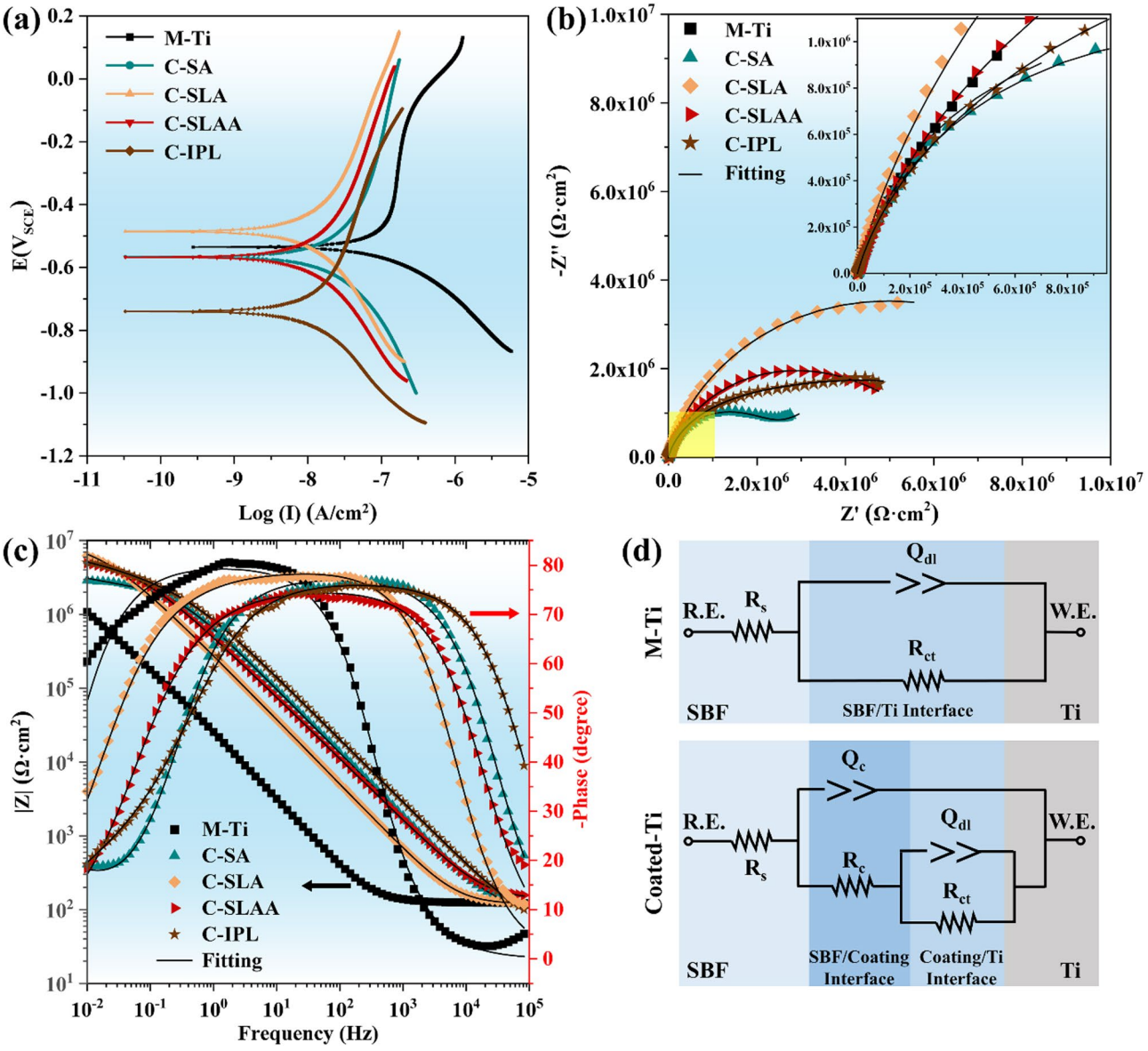

Fig. 7 Electrochemical performance evaluation of the samples. (**a**) Potentiodynamic polarization curves. (**b**) Nyquist plots and (**c**) Bode amplitude and phase angle plots of the impedance spectra. (**d**) Equivalent electrical circuits used to model impedance behaviors

Table 1 Electrochemical corrosion parameters derived from potentiodynamic polarization curves of the samples. Values are presented as mean ± standard deviation (SD), $n = 3$

Samples	E_{corr} (V)	I_{corr} ($\times 10^{-8}$, A/cm^2)	β_a (V·dec^{-1})	β_c (V·dec^{-1})	R_p (KΩ·cm^2)
M-Ti	-0.50 ± 0.03	41.33 ± 1.90	0.660 ± 0.146	0.127 ± 0.012	110.93 ± 9.31
C-SA	-0.56 ± 0.01	6.47 ± 1.21	0.219 ± 0.003	0.184 ± 0.003	683.78 ± 125.72
C-SLA	-0.48 ± 0.01	2.83 ± 0.11	0.222 ± 0.003	0.184 ± 0.001	1544.34 ± 62.14
C-SLAA	-0.56 ± 0.01	3.36 ± 0.17	0.217 ± 0.003	0.190 ± 0.002	1311.00 ± 67.57
C-IPL	-0.76 ± 0.03	3.66 ± 0.14	0.250 ± 0.003	0.172 ± 0.010	1213.70 ± 81.86

Table 2 EIS-fitted parameters of equivalent electrical circuits for the samples. Values are presented as mean ± standard deviation (SD), $n = 3$

Samples	R_s (Ω·cm^2)	Q_c ($\times 10^{-8}$ Ω^{-1}·cm^{-2}·S^{-n})	R_c (KΩ·cm^2)	Q_{dl} ($\times 10^{-7}$ Ω^{-1}·cm^{-2}·S^{-n})	R_{ct} (KΩ·cm^2)
M-Ti	119.47 ± 2.87	-	-	79.70 ± 2.70	2735.83 ± 431.90
C-SA	127.25 ± 21.43	21.85 ± 0.53	285.10 ± 85.23	3.85 ± 1.50	3076.25 ± 266.93
C-SLA	109.00 ± 12.45	72.41 ± 3.12	445.89 ± 83.57	1.35 ± 0.43	9501.05 ± 426.74
C-SLAA	133.60 ± 14.28	38.71 ± 5.48	552.26 ± 70.16	1.14 ± 0.19	5732.10 ± 659.31
C-IPL	83.59 ± 16.81	16.00 ± 2.01	331.13 ± 30.40	2.18 ± 0.43	6169.47 ± 577.35

As shown in Table 1, the E_{corr} values of the coated samples vary significantly despite their similar chemical compositions. Although the E_{corr} is a thermodynamic parameter and is primarily determined by the interaction between the material and the environment, surface roughness in actual testing may influence the true surface area of the electrode, leading to deviations in the measured E_{corr}. Rough surfaces increase the effective surface area of the sample, and this change can cause variations in the E_{corr}. The C-IPL sample has a rough surface, and its fine grain size further increases the effective surface area, resulting in a negative shift of its E_{corr}. Additionally, it is generally accepted that the negative E_{corr} indicates a higher likelihood of corrosion, and a larger I_{corr} represents a higher corrosion rate in PDP testing [45]. However, during analysis, inconsistencies may arise between E_{corr} and I_{corr} when determining the corrosion characteristics. In such cases, I_{corr} is used as a reference because it is more widely applicable and serves as a standard for evaluating the corrosion rate of materials, while E_{corr} merely describes the thermodynamic properties of the material. Additionally, it should be noted that the standard criteria for E_{corr} and I_{corr} are more applicable to pure metals or metallic conductive coatings. Since phosphate coatings are non-conductive, their presence alters the prerequisites for applying the Butler-Volmer equation used in PDP testing for the Ti substrate, i.e., no protective coating on the metal substrate surface for the anodic process [46]. Therefore, the results from the PDP curve and related corrosion parameters can only be used for qualitative assessment of the coatings corrosion resistance.

To further analyze the impact of substrate pretreatment on coating corrosion behavior, the EIS test was used to assess the samples in SBF. EIS, widely recognized as an effective method for evaluating corrosion characteristics, provides insights into the interface and structural properties of coatings on Ti substrates while preserving the stability of the coating surface [47]. Figure 7b shows the Nyquist plots of the samples, where high-frequency capacitive arcs represent the charge transfer resistance at the coating/electrolyte interface, while low-frequency arcs correspond to the resistance at the coating/substrate interface [48]. The larger capacitive arc radii of the coated samples indicate higher charge transfer resistance and enhanced corrosion resistance compared to M-Ti. The C-SLA sample exhibits the largest capacitive arc diameter, signifying the highest corrosion resistance. Additionally, the Bode amplitude and phase-angle plots (Fig. 7c) reveal distinct relaxation characteristics of the samples. M-Ti displays a single time constant, whereas the coated samples show two relaxation time constants, suggesting the presence of two interfaces: electrolyte/coating and coating/substrate. Moreover, the impedance responses, as indicated by|Z| values at low frequency (10^{-2} Hz) and phase angle values at high frequency (10^5 Hz), demonstrate superior corrosion resistance of the coated samples compared to M-Ti, consistent with the PDP results.

From the EIS plots, two equivalent electrical circuits (EEC), $R_s(Q_{dl}R_{ct})$ and $R_s(Q_c(R_c(Q_{dl}R_{ct})))$ were used to model the impedance data, as shown in Fig. 7d. The components R_s, Q_{dl}, and R_{ct} represent the solution resistance, the capacitance of the electric double layer, and the charge transfer resistance, respectively. Q_c and R_c, specific to the coated samples, denote the coating capacitance and the resistance, respectively [49]. The chi-squared values (χ^2) are below 10^{-3}, validating the excellent fit of the EEC to the actual corrosion systems. The fitted parameters of the EEC components are summarized in Table 2. The resistance values (R_c and R_{ct}) of the samples exhibit a trend consistent with R_p in the

PDP tests. Overall, the coatings can effectively inhibit the penetration of corrosion ions, enhancing corrosion resistance. In addition, the fitted results confirm superior corrosion resistance of the C-SLA, C-SLAA, and C-IPL samples compared to C-SA. This improvement is attributed to the synergistic effect of the coating and the rough interface between the coating and substrate.

Controlling bacterial infection

The physical characteristics of material surfaces, such as microstructure, roughness, and wettability, play a critical role in influencing bacterial adhesion behavior during the initial phase of implantation [50]. Therefore, evaluating bacterial adhesion provides essential insights for designing effective surface modifications. Once bacteria adhere to and colonize a material surface, they proliferate and aggregate to form biofilms, typically within 24 h. Bacterial biofilms can lead to inflammatory infections, posing significant challenges to the safety and stability of implants [51]. In this study, 24 h was selected as the critical time point to evaluate the biofilm inhibition properties of the coatings.

Figure 8 illustrates the bacterial growth inhibition effects of various coatings against *S. aureus* and *E. coli* after 24 h of culture, with the M-Ti sample serving as the control. As shown in Fig. 8a, the solid agar plate corresponding to the M-Ti sample displays numerous live bacterial colonies, indicating that bacteria grow normally on the sample surface after 24 h of incubation. In contrast, the agar plates for the four coated samples exhibit a significant reduction in the number of live bacterial colonies, suggesting reduced bacteria growth and proliferation upon contact with the surfaces. The quantitative results in Fig. 8b show that the inhibition rates against *S. aureus* for the C-SA, C-SLA, and C-SLAA samples reach 83.75%, 82.24%, and 83.11%, respectively, while the C-IPL sample further increases the rate to 91.09%. Similarly, for *E. coli*, the inhibition rates for the C-SA, C-SLA, and C-SLAA are 75.75%, 71.99%, and 73.38%, respectively, with the C-IPL sample achieving a higher inhibition rate of 84.04% (Fig. 8c). These results indicate no statistically significant differences in bacterial growth inhibition properties among the C-SA, C-SLA, and C-SLAA samples, while the C-IPL sample exhibits a markedly enhanced controlling bacterial infection effect. The FE-SEM images in Fig. 8d further depict the quantity and morphology of *S. aureus* and *E. coli* adhered to the sample surfaces after 24 h. On the M-Ti surface, a larger number of bacteria are observed, with both *S. aureus* (spherical) and *E. coli* (rod-shaped) maintaining intact morphologies, smooth surfaces, and complete cell membranes. In contrast, only sparse bacterial adhesion is observed on the four coated surfaces, with some bacteria exhibiting irregular collapse, indicating substantial structural damage and rupture or dissolution of the cell membranes.

These findings indicate that the SrZnP coatings effectively inhibit biofilm formation by *S. aureus* and *E. coli*, demonstrating notable bacterial growth inhibition properties. The controlling bacterial infection performance of phosphate coatings is closely related to their ion release behavior, particularly that of metallic cations. The ions release profiles from the coated samples in 0.9 wt% NaCl solution are presented in Fig. S3, demonstrating a general increase in ion concentrations over time. At each time point, the C-IPL sample exhibits the highest ion release, while C-SLA and C-SLAA show comparable release levels, and C-SA displays the lowest. This trend is strongly correlated with the surface morphology of the four samples. The rough surfaces of C-SLA, C-SLAA, and C-IPL, inherited from the sandblasted substrate, provide a larger contact area with the immersion solution, thereby accelerating ion release. Notably, the fine and uniformly distributed crystalline structures on the C-IPL surface further contribute to its highest ion release rate. Moreover, after 24 h of immersion, the Zn^{2+} ion concentrations released from all coated samples exceed the minimum bactericidal concentration (MBC) of Zn^{2+}, which is 0.65 ppm [52]. This suggests that the released Zn^{2+} ions may effectively inhibit bacterial growth, contributing to the antibacterial properties of the coatings. Previous studies have demonstrated that the antibacterial efficacy of Sr-containing phosphate coatings primarily depends on the release of Zn^{2+} ions, as Sr^{2+} ions exhibit negligible antibacterial effects [15]. Zn^{2+} ions penetrate bacterial cell membranes and induce the generation of reactive oxygen species, which disrupt membrane integrity, thereby inhibiting bacterial adhesion, proliferation, and biofilm formation [53]. Additionally, compared with the C-SA sample, the rougher surfaces of the C-SLA and C-SLAA samples exhibit slightly reduced bacterial growth inhibition properties, likely attributable to increased surface roughness, which offers more surface area for bacterial adhesion. Although the C-IPL sample also possesses a roughened surface, its microstructure is defined by significantly smaller crystal sizes and uniformly aligned nano-topological structure. This unique topography, featuring a ripple-like surface, may exert a contact-inhibition effect that compromises bacterial cell integrity [19]. Consequently, the synergistic effects of the nano-topological structure and Zn^{2+} ions enable the C-IPL sample to achieve superior bacterial growth inhibition properties.

Some studies have reported that phosphate coatings on Ti surfaces also exhibit superior bacterial inhibition rates, such as Zn/Sr-doped CaP coatings (*S. aureus*: 90%, *E. coli*: 95%) and ZnP/ZnO hybrid coatings (*S. aureus*: 98%, *E. coli*: 90%) [4, 19]. However, satisfactory bacterial

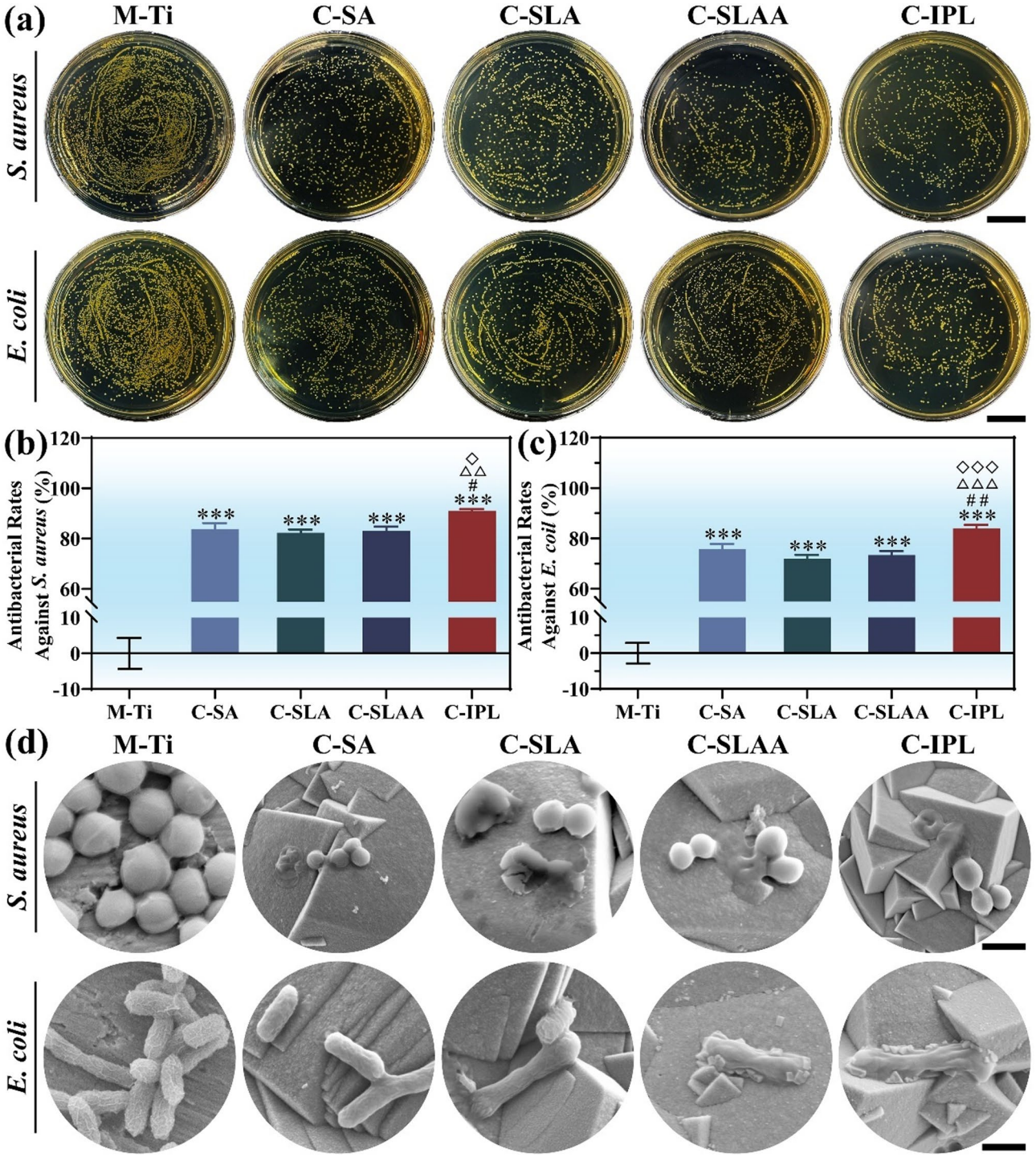

Fig. 8 Bacterial growth inhibition properties of the samples after 24 h of incubation. (**a**) Agar plate images show the recultivation of colonies dissociated from the sample surfaces (scale bar: 2 cm). Quantitative inhibition rates for (**b**) *S. aureus* and (**c**) *E. coli* ($n = 3$). (**d**) SEM images depicting the morphology and adhesion of *S. aureus* and *E. coli* on different sample surfaces (scale bar: 1 μm). *, #, △, and ◇ indicate $P < 0.05$, **, while ##, △△, and ◇◇ represent $P < 0.01$, and ***, ###, △△△, and ◇◇◇ indicate $P < 0.001$, corresponding to comparisons with M-Ti, C-SA, C-SLA, and C-SLAA, respectively

inhibition rates (*S. aureus*: 91.09%, *E. coli*: 84.04%) can still be observed from the SrZnP coating (C-IPL) in this study. The slightly lower inhibition rates may be due to the high crystallinity of the PCC coating, which slows down the release of Zn^{2+} ions. A moderate release of Zn^{2+} ions can also better balance bacterial inhibition performance and cell compatibility. Furthermore, we previously developed a Zn-doped SrCaP coating, which

achieved bacterial inhibition rates of 83.01% and 71.28% for *S. aureus* and *E. coli*, respectively [15]. In contrast, the bacterial inhibition performance of the SrZnP coating (C-IPL) modified through ions preloading in this study has been significantly improved.

Cell adhesion and proliferation

The surface characteristics of the coatings, including their micro- and nano-structures, roughness, wettability, and other physical properties, significantly influence cellular adhesion, proliferation, and differentiation [54]. To evaluate these effects, in vitro cell experiments were conducted to investigate the interaction of different samples with cell behaviors. The adhesion and growth of osteoblasts on the implant surface of the implant are fundamental for subsequent functional expression, such as proliferation and osteogenic differentiation [55]. Figure 9a presents the FE-SEM images of BMSCs adhesion

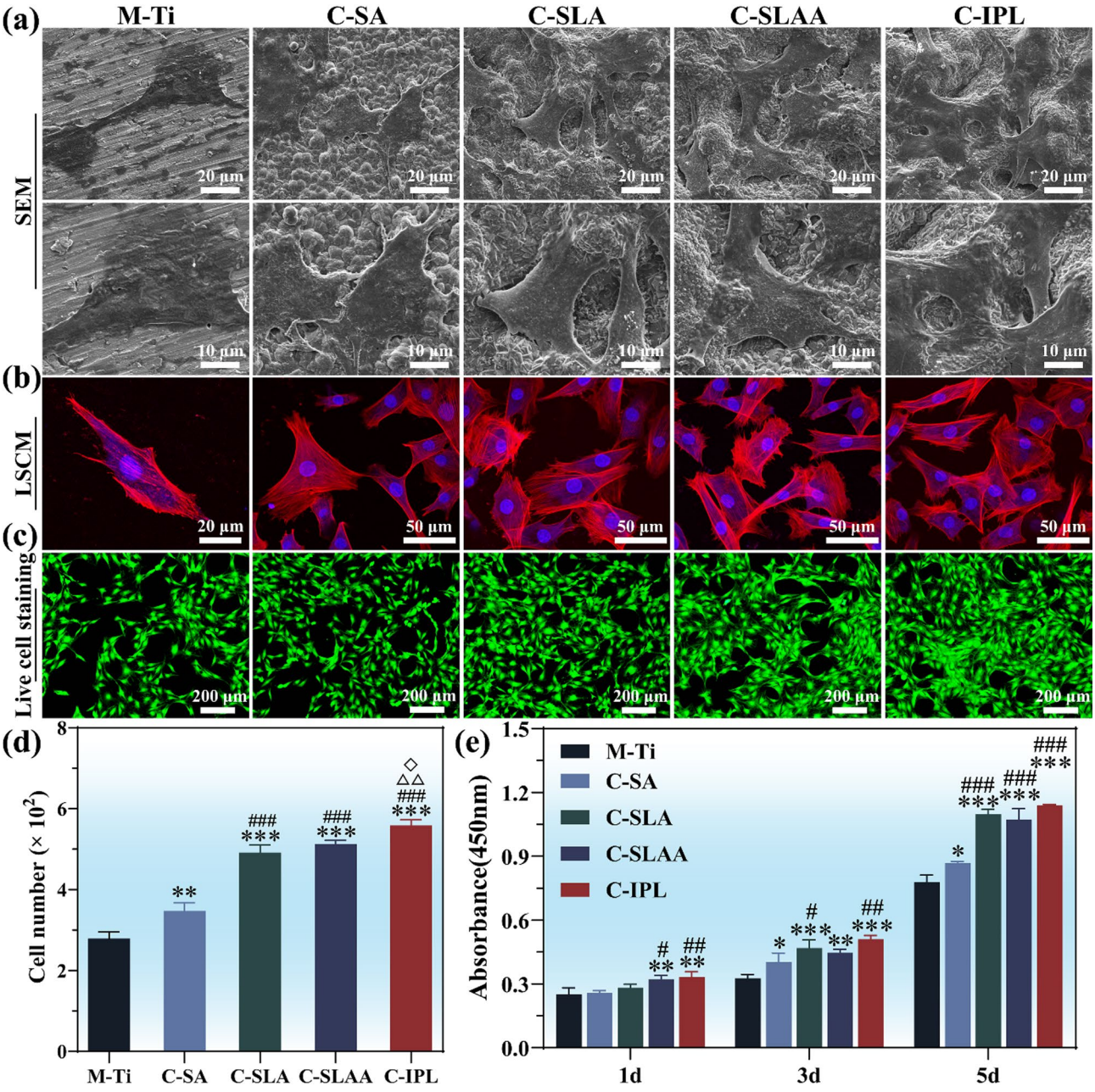

Fig. 9 Morphologies of BMSCs adhered to the surfaces of different samples after 24 h of incubation, observed via (**a**) SEM, (**b**) LSCM, and (**c**) Live-cell staining. (**d**) Quantitative analysis of live-cell counts using ImageJ software ($n = 3$). (**e**) Proliferation of BMSCs on various samples, evaluated through the CCK-8 assay after 1, 3, and 5 days of culture ($n = 3$). *, #, △, and ◇ indicate $P < 0.05$, **, while ##, △△, and ◇◇ represent $P < 0.01$, and ***, ###, △△△, and ◇◇◇ indicate $P < 0.001$, corresponding to comparisons with M-Ti, C-SA, C-SLA, and C-SLAA, respectively

morphologies on the surfaces of M-Ti and the four coated samples after 2 days of culture. The cells adhesion well and display a spreading state on all sample surfaces. On M-Ti, the cells appear spindle-shaped with minimal pseudopod extension. In contrast, the cells on the coated samples exhibit a polygonal morphology with pronounced filamentous or plate-like pseudopods. These pseudopods are closely attached to the prominent crystal edges of the coatings. Similar adhesion morphologies are observed in the LSCM images (Fig. 9b), where F-actin and nuclei are fluorescently stained with phalloidin (red) and DAPI (blue), respectively. Evident pseudopod growth, aggregation, and interconnected pseudopods are visible on the coated sample surfaces. No significant difference in single-cell adhesion or spreading is observed among the four coated samples.

Cell proliferation, a critical activity following adhesion, facilitates an increase in cell numbers and subsequent functional expression. Live-cell staining images (Fig. 9c) demonstrate a higher number of viable cells (green) on the coated samples compared to M-Ti, with the C-IPL sample exhibiting the highest cell viability. Quantitative analysis of cell viability (Fig. 9d) further confirms this trend. Additionally, cell proliferation assessed by CCK-8 (Fig. 9e) reveals a time-dependent increase in OD values for all samples, indicating an increase in viable cell numbers over the culture period.

The results of cell adhesion and proliferation demonstrate that the coatings exhibit excellent biocompatibility, effectively promoting cell adhesion, spreading, and growth. This is primarily attributed to the favorable wettability of the coatings and their roughened surfaces. The surface microstructure plays a crucial role in regulating cell behavior, as the prominent crystal edges on the coatings provide additional anchoring points for pseudopod extension, thereby enhancing cell attachment and spreading [56]. These processes are foundational for subsequent cell migration, growth, proliferation, and functional expression. The enhanced roughness and multi-level microstructures of the C-SLA, C-SLAA, and C-IPL samples, resulting from sandblasting treatment, further facilitate cell adhesion and spreading, supporting later stages of cell activity. However, it is worth noting that both excessively high and low roughness levels can adversely affect cell adhesion. Overly rough surfaces may limit available space for cell spreading, hinder growth, and potentially lead to cell apoptosis [57]. Conversely, excessively smooth surfaces may fail to provide sufficient anchorage for cells. Among the tested samples, the C-IPL sample, characterized by its moderate roughness, exhibits the most favorable performance in promoting cell adhesion and proliferation.

Cell differentiation assays

The main purpose of this study is to enhance the osteogenic ability of Ti implants by constructing phosphate coatings on their surfaces. Therefore, the effects of the coatings on the osteogenic differentiation of BMSCs are evaluated by analyzing the expression of osteogenic-related genes and proteins. After 7 days of culture, ALP staining results (Fig. 10a) and quantitative data (Fig. 10c) show that the coated groups exhibit a deeper purple color compared to M-Ti, indicating significant upregulation of ALP expression in BMSCs, particularly in the C-IPL sample. ARS staining can be used to visualize calcium nodules deposited in the extracellular matrix of BMSCs following osteogenic differentiation. The staining intensity directly reflects the degree of osteogenic differentiation in BMSCs. ARS staining results of BMSCs cultured on different sample surfaces for 14 days are shown in Fig. 10b, with corresponding quantitative data presented in Fig. 10d. Lighter staining and fewer calcium nodules are observed on M-Ti, whereas coated sample surfaces exhibit more intense red staining and abundant calcium nodules. These results demonstrate that the coated samples better induced extracellular matrix mineralization, particularly in the C-IPL sample. These findings are further confirmed by immunofluorescence staining of Runx2 and OPN (Fig. 10e–h). The cells on the C-IPL sample show the strongest fluorescence intensity.

Specific gene and protein markers involved in bone repair and formation can provide critical evidence for material-induced bone regeneration. ALP is a marker of early-stage osteogenic differentiation, providing free phosphate for the growth of hydroxyapatite and extracellular matrix mineralization [58]. It plays a crucial role in osteoblast differentiation, chondrocyte maturation, and the production of bone matrix proteins [59]. Col-I, expressed in the early and middle stages of osteogenic differentiation, plays a crucial role in extracellular matrix mineralization by serving as a nucleation site for hydroxyapatite crystals and promoting calcium deposition [60]. OCN is a marker of late-stage osteogenic differentiation. As a critical extracellular matrix component, OCN interacts with vitamin and calcium ions to regulate bone growth and metabolism [61]. As shown in Fig. 10i–k, the coated samples induce higher expression levels of bone formation-related genes compared to M-Ti. During the 14-day culture period, gene expression levels on all samples are gradually increased. The C-IPL sample stimulates the highest expression levels of osteogenesis-related genes. Despite no notable differences in the expression of ALP and Col-I genes among C-SA, C-SLA, and C-SLAA groups on day 7, significant increases in both genes expression are observed in the C-IPL sample compared with those in other groups. By day 14, the samples with rougher surfaces (C-SLA,

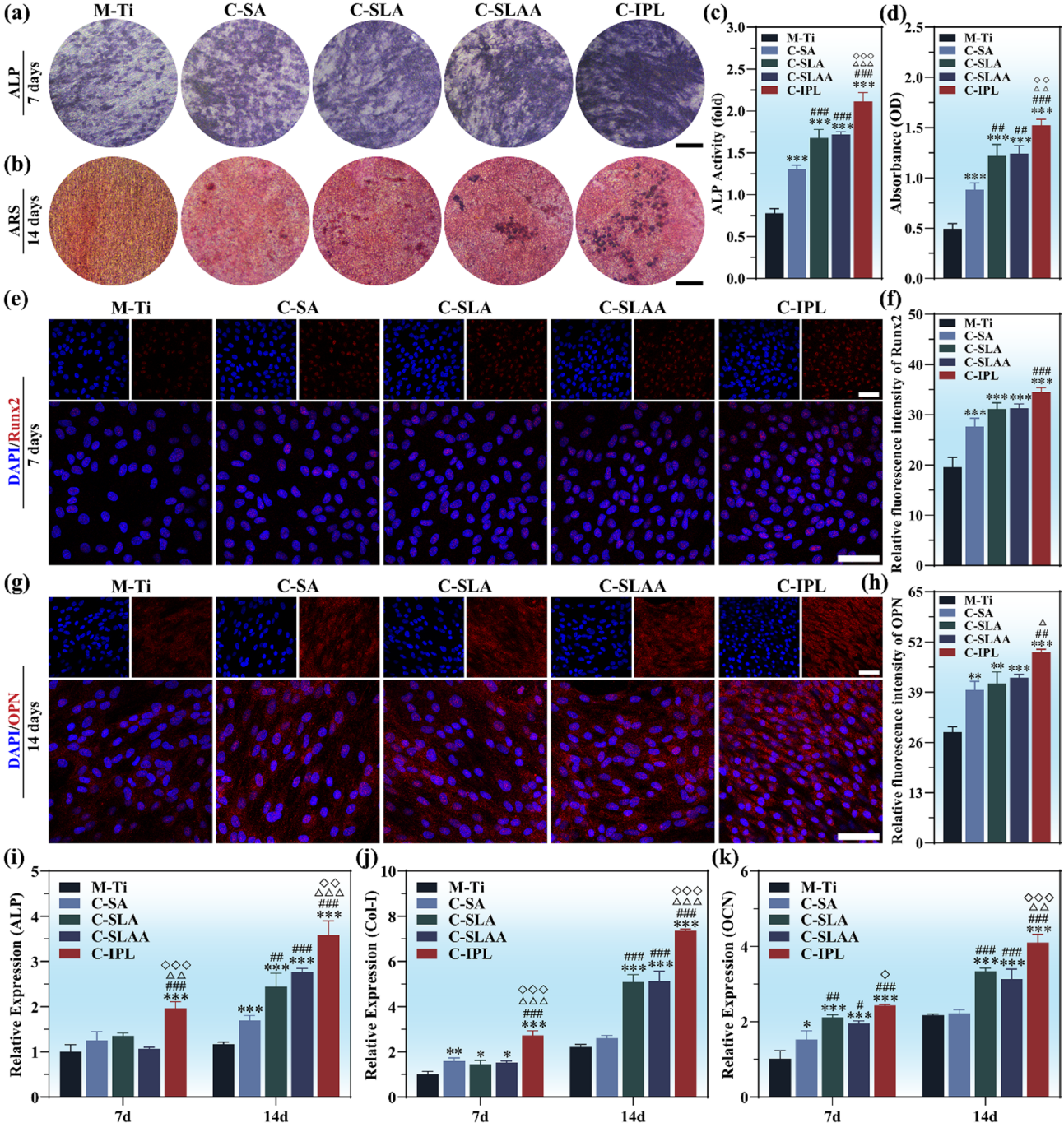

Fig. 10 Osteogenic behavior of BMSCs in vitro. (**a**) Alkaline phosphatase (ALP) and (**b**) Alizarin red s (ARS) staining at 7 and 14 days, respectively (scale bar: 200 μm). (**c**) and (**d**) show the quantitative analysis of ALP and ARS staining, respectively ($n = 3$). (**e**) Immunofluorescence staining images and (**f**) corresponding fluorescence intensity analysis of Runx2 at 7 days ($n = 3$, scale bar: 50 μm). (**g**) Immunofluorescence staining images and (**h**) corresponding fluorescence intensity analysis of OPN at 14 days ($n = 3$, scale bar: 50 μm). (**i**–**k**) RT-PCR analysis of osteogenic-related gene expression in BMSCs cultured on different samples at 7 and 14 days (ALP, Col-I, and OCN). *, #, △, and ◇ indicate $P < 0.05$, **, while ##, △△, and ◇◇ represent $P < 0.01$, and ***, ###, △△△, and ◇◇◇ indicate $P < 0.001$, corresponding to comparisons with M-Ti, C-SA, C-SLA, and C-SLAA, respectively

C-SLAA, and C-IPL) exhibit significantly higher ALP and Col-I expression levels than the C-SA sample. Moreover, the mRNA levels of OCN in the C-SLA, C-SLAA, and C-IPL samples are higher than those in the C-SA sample and are substantially upregulated with prolonged culture time, with the highest expression in the C-IPL group. The RT-qPCR result of OCN (a biomarker of late-stage cell mineralization), is consistent with ARS staining, which also reveals the largest area of mineralized deposition and the highest number of calcium nodules within the

C-IPL group. These findings could be partly attributed to the rough surfaces of C-SA, C-SLA, and C-SLAA, which mimic the microenvironment of natural bone tissue, thereby enhancing the adhesion of BMSCs to Ti surface and facilitating their differentiation into osteoblasts. Particularly, the C-IPL sample, characterized by its uniform micro-nano structure, exhibits a superior capacity for promoting BMSCs differentiation and further inducing the mineralization of the extracellular matrix.

The surface characteristics of Ti implants, including microstructure, roughness, wettability, and ion release, are critical in influencing stem cell osteogenic differentiation and determining the in vivo integration efficiency of Ti implants [62]. Moderate surface roughness can create a microenvironment resembling natural bone tissue, enhancing stem cell recognition and adhesion to the Ti surface, thereby supporting osteogenic differentiation [63]. Studies have shown that microscale surface roughness promotes the expression of osteogenesis-related genes. In addition, a roughened surface can stimulate integrin receptors on cells, initiating mechanotransduction pathways such as focal adhesion kinase (FAK) signaling and Wnt/β-catenin signaling [64]. These pathways regulate the cytoskeleton and activate biochemical signaling cascades essential for osteogenic differentiation. Moreover, an appropriately rough surface facilitates blood clot formation, enhances the recruitment and adhesion of osteoblasts, and strengthens the interface between bone tissue and implants [65]. Regarding wettability, hydrophilic surfaces can adsorb larger amounts of serum proteins, such as fibronectin and OPN, which are crucial for cell adhesion and signal transduction [66]. These proteins can enhance cell adhesion, spreading, and osteogenic differentiation. The sustained release of bioactive ions from the SrZnP coatings (Fig. S3) plays a crucial role in regulating bone metabolism. The synergistic release of Sr and Zn exerts multi-dimensional regulatory effects, including the activation of osteogenic signaling pathways at the molecular level, enhancement of extracellular matrix mineralization, and effective inhibition of osteoclastic activity at the functional level [18, 20]. Notably, the P component serves as a key regulatory factor in bone matrix mineralization by activating phosphate transport systems specific to osteoblasts [24]. Studies have demonstrated that variations in phosphate concentration gradients in the in vitro culture environment positively regulate the transcriptional activity of the OPN gene. Furthermore, a significant dose-dependent relationship has been observed between phosphate concentration thresholds and the efficiency of mineralized nodule formation [67]. Consequently, the combination of surface roughness, hydrophilicity, and ions release for SrZnP coatings can produce a synergistic effect that further promotes osteogenic differentiation and bone integration.

Conclusions

This study investigates the optimizing effect of Sr/Zn ions preloading and micro/nanostructured surface modifications on the structure and surface characteristics of SrZnP conversion coatings on Ti substrates. The micro/nanostructured surface modifications reduced the thickness and simultaneously enhanced the adhesion strength of the coatings characterized by the $SrZn_2(PO_4)_2$ phase and a cubic crystal morphology. Surface microstructural modifications of Ti achieved through SA, SLA, and SLAA treatments did not exhibit a significant influence on interface reactions. In contrast, the IPL treatment incorporating Sr^{2+} and Zn^{2+} ions activated the interactions at the coating-Ti interface during chemical conversion. This approach facilitated the in-situ release of coating-component ions (Sr^{2+} and Zn^{2+}), significantly increasing the density of nucleation sites on Ti surfaces, and restricting the growth of SrZnP crystals, whereby smaller and more uniformly sized crystals were finally formed. The coatings on IPL-Ti exhibited moderate surface roughness, enhanced wettability, and excellent corrosion resistance, achieving the highest bacterial growth inhibition property also in terms of the synergistic effects of its topography and antibiotic constituents. Meanwhile, the crystal-refined coatings further effectively facilitated BMSCs adhesion and proliferation, as well as osteogenic differentiation of BMSCs by promoting matrix mineralization, and upregulating the expression of ALP and osteogenesis-related genes, thereby proving the superior osteogenic activity. The strategy of interface reaction regulation by ions preloading and micro/nanostructured surface modification facilitates the potential application of Sr/Zn-phosphate conversion coatings for repairing infected bone defects.

Supplementary Information

The online version contains supplementary material available at https://doi.org/10.1186/s12951-025-03443-6.

Supplementary Material 1

Acknowledgements

This work was supported by the National Key Research and Development Program (Additive Manufacturing and Laser Manufacturing Key Special Project) (2023YFB4606705), National Natural Science Foundation of China (Grant Nos. 52201299), Natural Science Foundation of Shandong Province (Grant Nos. ZR2022QE192, ZR2023MH209, and ZR2024QE204), China Postdoctoral Science Foundation (Grant Nos. 2024M751892), Shandong Province Medical and Health Technology Project (Grant Nos. 202404070683), and Innovation ability improvement project of scientific and technological company Shandong Province (2022TSGC2396).

Author contributions

Kangqing Zuo: Writing– original draft, Methodology, Investigation, Conceptualization. Aonan Li: Methodology, Data curation. Taoning Si: Validation, Data curation. Weiyi Lei: Methodology, Investigation, Data

curation. Yusheng Liu: Visualization, Validation. Linbo Zhang: Methodology, Investigation. Taixing Zhang: Methodology, Investigation. Guiyong Xiao: Formal analysis, Funding acquisition. Yupeng Lu: Project administration, Supervision. Ningbo Li: Writing– review & editing, Project administration, Funding acquisition.

Data availability
No datasets were generated or analysed during the current study.

Declarations

Ethics approval and consent to participate
Not applicable.

Consent for publication
All authors have read and approved the manuscript.

Competing interests
The authors declare no competing interests.

Author details
[1]Department of Stomatology, Shandong Provincial Hospital Affiliated to Shandong First Medical University, Ji'nan 250021, Shandong Province, P. R. China
[2]School of Stomatology, Shandong First Medical University & Shandong Academy of Medical Sciences, Ji'nan 250117, Shandong Province, P. R. China
[3]Medical Science and Technology Innovation Center, Shandong First Medical University & Shandong Academy of Medical Sciences, Ji'nan 250117, Shandong Province, P. R. China
[4]Key Laboratory for Liquid-Solid Structural Evolution and Processing of Materials, Ministry of Education, Shandong University, Ji'nan 250061, Shandong Province, P. R. China
[5]School of Materials Science and Engineering, Shandong University, Ji'nan 250061, Shandong Province, P. R. China

Received: 22 January 2025 / Accepted: 5 May 2025
Published online: 19 May 2025

References

1. Jiang PL, Zhang YM, Shi B, Zhang LH, Huang QL, Yang Y, Tang PF, Lin CJ. Advanced surface engineering of titanium materials for biomedical applications: from static modification to dynamic responsive regulation. Bioact Mater. 2023;27:15–57.
2. Kim JC, Lee M, Yeo IL. Three interfaces of the dental implant system and their clinical effects on hard and soft tissues. Mater Horiz (2022) 1387–411.
3. Dong JY, Chen FM, Yao YY, Wu CC, Ye SL, Ma ZW, Yuan HP, Shao D, Wang L, Wang YJ. Bioactive mesoporous silica nanoparticle-functionalized titanium implants with controllable antimicrobial peptide release potentiate the regulation of inflammation and osseointegration. Biomaterials. 2024;305:122465.
4. Zhao FL, Gao A, Liao Q, Li YY, Ullah I, Zhao Y, Ren XX, Tong LP, Li X, Zheng YD, Chu PK, Wang HY. Balancing the Anti-Bacterial and Pro-Osteogenic properties of Ti-Based implants by partial conversion of ZnO nanorods into hybrid zinc phosphate nanostructures. Adv Funct Mater. 2024;34:2311812.
5. Zhang HM, Yuan Y, Xue HX, Yu RP, Jin XY, Wu XL, Huang H. Reprogramming mitochondrial metabolism of macrophages by miRNA-released microporous coatings to prevent peri-implantitis. J Nanobiotechnol. 2023;21:485.
6. Zhang LC, Chen LY. A review on biomedical titanium alloys: recent progress and prospect. Adv Eng Mater. 2019;21:1801215.
7. Zhang LC, Chen LY, Wang LQ. Surface modification of titanium and titanium alloys: technologies, developments, and future interests. Adv Eng Mater. 2020;22:1901258.
8. Zhang GM, Deng LH, Jiang ZJ, Xiang G, Zeng ZT, Zhang HQ, Wang YJ. Titanium nanoparticles released from orthopedic implants induce muscle fibrosis via activation of SNAI2. J Nanobiotechnol. 2024;22:522.
9. Han JY, Ma QL, An YX, Wu F, Zhao YQ, Wu GY, Wang J. The current status of stimuli-responsive nanotechnologies on orthopedic titanium implant surfaces. J Nanobiotechnol. 2023;21:277.
10. Yang K, Deng RY, Wang CF, Wu SL, Cui ZD, Zheng YF, Li ZY, Jiang H, Zhu SL, Chu PK, Liu XM. CuO/ZnO heterojunction nanofilm for effective photocatalytic disinfection. Surf Interfaces. 2024;53:105023.
11. Yu YT, Lee WH, Hsieh SF, Ou SF. Effects of hydroxyapatite size on the drug release characteristics of drug-containing coatings. Prog Org Coat. 2024;195:108600.
12. Lin MH, Yu YT, Ou SF. Formation of calcium-phosphate-based coatings on titanium by laser-induced deposition in liquid environment. Appl Surf Sci. 2023;641:158448.
13. Huang CC, Yang TH, Lin MH, Fan FY, Ou SF. Role of graphene in bactericidal activity and bioactivity of a Zn/graphene/ Chitosan coating. Prog Org Coat. 2024;196:108761.
14. Liu B, Zhang X, Xiao GY, Lu YP. Phosphate chemical conversion coatings on metallic substrates for biomedical application: A review. Mater Sci Eng C. 2015;47:97–104.
15. Zuo KQ, Wang LL, Wang ZH, Yin YX, Du CM, Liu B, Sun LY, Li XY, Xiao GY, Lu YP. Zinc-Doping induces evolution of biocompatible Strontium-Calcium-Phosphate conversion coating on titanium to improve antibacterial property. ACS Appl Mater Interfaces. 2022;14:7690–705.
16. Li YB, Zhang HQ, Lu YP, Yang XJ, Wang GD, Wang YY, Tang KL, Huang SY, Xiao GY. Construction of magnesium phosphate chemical conversion coatings with different microstructures on titanium to enhance osteogenesis and angiogenesis. ACS Appl Mater Interfaces. 2024;16:21672–88.
17. Shi YB, Tao WD, Yang WJ, Wang L, Qiu ZN, Qu XL, Dang JY, He JK, Fan HB. Calcium phosphate coating enhances osteointegration of melt electrowritten scaffold by regulating macrophage polarization. J Nanobiotechnol. 2024;22:47.
18. Molenda M, Kolmas J. The role of zinc in bone tissue health and Regeneration-a review, biol. Trace Elem Res. 2023;201:5640–51.
19. Wang YK, Teng WSY, Zhang ZJ, Zhou XZ, Ye YX, Lin P, Liu A, Wu Y, Li BH, Zhang CD, Yang XY, Li WX, Yu XH, Gou ZR, Ye ZM. A trilogy antimicrobial strategy for multiple infections of orthopedic implants throughout their life cycle. Bioact Mater. 2021;6:1853–66.
20. Rossi AL, Moldovan S, Querido W, Rossi A, Werckmann J, Ersen O, Farina M. Effect of strontium Ranelate on bone mineral: analysis of nanoscale compositional changes. Micron. 2014;56:29–36.
21. Ciosek Z, Kot K, Kosik-Bogacka D, Lanocha-Arendarczyk N, Rotter I. The effects of calcium, magnesium, phosphorus, fluoride, and lead on bone tissue. Biomolecules. 2021;11:506.
22. Takeda E, Yamamoto H, Yamanaka-Okumura H, Taketani Y. Dietary phosphorus in bone health and quality of life. Nutr Rev. 2012;70:311–21.
23. Jeong J, Kim JH, Shim JH, Hwang NS, Heo CY. Bioactive calcium phosphate materials and applications in bone regeneration. Biomater Res. 2019;23:4.
24. Zhang R, Lu YB, Ye L, Yuan BZ, Yu SB, Qin CL, Xie YX, Gao T, Drezner MK, Bonewald LF, Feng JQ. Unique roles of phosphorus in endochondral bone formation and osteocyte maturation. J Bone Min Res. 2011;26:1047–56.
25. Tada H, Nemoto E, Foster BL, Somerman MJ, Shimauchi H. Phosphate increases bone morphogenetic protein-2 expression through cAMP-dependent protein kinase and ERK1/2 pathways in human dental pulp cells. Bone. 2011;48:1409–16.
26. Zhao DW, Liu C, Zuo KQ, Su P, Li LB, Xiao GY, Cheng L. Strontium-zinc phosphate chemical conversion coating improves the osseointegration of titanium implants by regulating macrophage polarization. Chem Eng J. 2021;408:127362.
27. Kozelskaya AI, Frueh A, Rutkowski S, Goreninskii SI, Verzunova KN, Soldatova EA, Dorozhko EV, Frueh J, Bakina OV, Buldakov MA, Choinzonov EL, Brizhan LK, Kerimov AA, Khominets I, Davydov D, Tverdokhlebov SI. Antibacterial double-layer calcium phosphate/chitosan composite coating on metal implants for tissue engineering, Colloids Surf., A 705 (2025) 135652.
28. Kim KT, Nisar SS, Choe HC. Mechanical octacalcium phosphate coatings on the plasma electrolytic oxidized pure titanium for bio-implant use. Surf Coat Technol. 2024;480:130602.
29. Safari-Gezaz M, Parhizkar M, Asghari E. Investigation of the structural properties of Si4+-doped HAP coatings on Ti-6Al-4V substrate as a corrosion barrier in biomedical media. Colloids Surf A. 2024;699:134742.
30. Narayanan TSNS. Surface pretreatment by phosphate conversion coatings-A review, rev. Adv Mater Sci. 2005;9:130–77.
31. Song MS, Li RW, Qiu Y, Tuipulotu DE, Man SM, Birbilis N, Smith PN, Cole I, Kaplan DL, Chen XB. Gallium-Strontium phosphate conversion coatings for promoting infection prevention and biocompatibility of magnesium for orthopedic applications, ACS biomater. Sci Eng. 2022;8:2709–23.

32. Skoláková A, Pinc J, Jablonská E, Skoláková T, Vertát P, Janebová B, Kutová A, Capek J, Hosová K, Vojtech D, Kubásek J. A zinc phosphate layered biodegradable Zn-0.8Mg-0.2Sr alloy: characterization and mechanism of Hopeite formation. Surf Coat Technol. 2024;487:130986.
33. Zhou LQ, You JC, Wang ZY, Gu Y, Chen DH, Lin B, Zhao X, Lin JM, Lin JX. Liu, 3D printing monetite-coated Ti-6Al-4V surface with osteoimmunomodulatory function to enhance osteogenesis, biomater. Adv. 2022;134:112562.
34. Zhao XC, Dong SF, Ge B, Huang BX, Ma J, Chen H, Hao XH, Wang CZ. Effects of temperature and voltage on formation of electrolysis induced chemical conversion coating on titanium surface. Surf Coat Technol. 2018;354:330–41.
35. Liu B, Xiao GY, Jiang CC, Zheng YZ, Wang LL, Lu YP. Formation initiation and structural changes of phosphate conversion coating on titanium induced by galvanic coupling and Fe2 + ions. RSC Adv. 2016;6:75365–75.
36. Li YJ, Xu WH, Li NB, Ma Z, Huang BX, Ma J, Chen H, Hao XH, Zhao XC. Effect of different galvanic coupling methods on the surface chemical transformation of TC4 titanium alloy. Surf Coat Technol. 2024;478:130483.
37. Zhang X, Xiao GY, Zhao XC, He K, Xu WH, Lu YP. Rapid early formation and crystal refinement of chemical conversion Hopeite coatings induced by substrate sandblasting. New J Chem. 2015;39:7942–7.
38. Bai L, Chen PR, Zhao Y, Hang RY, Yao XH, Tang B, Liu CS, Xiao Y, Hang RQ. A micro/nano-biomimetic coating on titanium orchestrates osteo/angiogenesis and osteoimmunomodulation for advanced osseointegration. Biomaterials. 2021;278:121162.
39. Breviglieri ST, Cavalheiro ÉTG, Chierice GO. Correlation between ionic radius and thermal decomposition of Fe(II), Co(II), Ni(II), Cu(II) and Zn(II) diethanoldithiocarbamates, thermochim. Acta. 2000;356:79–84.
40. Zhang WB, Shen YH, Pan HB, Lin KL, Liu XG, Darvell BW, Lu WW, Chang JA, Deng LF, Wang DP, Huang WH. Effects of strontium in modified biomaterials. Acta Biomater. 2011;7:800–8.
41. Turk S, Altinsoy I, Efe GC, Ipek M, Ozacar M, Bindal C. A comparison of pretreatments on hydroxyapatite formation on Ti by biomimetic method. J Aust Ceram Soc. 2018;54:533–43.
42. Souza JCM, Sordi MB, Kanazawa M, Ravindran S, Henriques B, Silva FS, Aparicio C, Cooper LF. Nano-scale modification of titanium implant surfaces to enhance osseointegration. Acta Biomater. 2019;94:112–31.
43. Rupp F, Gittens RA, Scheideler L, Marmur A, Boyan BD, Schwartz Z, Geis-Gerstorfer J. A review on the wettability of dental implant surfaces I: theoretical and experimental aspects. Acta Biomater. 2014;10:2894–906.
44. Shokouhfar M, Dehghanian C, Montazeri M, Baradaran A. Preparation of ceramic coating on Ti substrate by plasma electrolytic oxidation in different electrolytes and evaluation of its corrosion resistance: part II. Appl Surf Sci. 2012;258:2416–23.
45. Bordbar-Khiabani A, Ebrahimi S, Yarmand B. In-vitro corrosion and bioactivity behavior of tailored calcium phosphate-containing zinc oxide coating prepared by plasma electrolytic oxidation. Corros Sci. 2020;173:108781.
46. Duan GQ, Yang LX, Liao SJ, Zhang CY, Lu XP, Yang YE, Zhang B, Wei Y, Zhang T, Yu BX, Zhang XC, Wang FH. Designing for the chemical conversion coating with high corrosion resistance and low electrical contact resistance on AZ91D magnesium alloy. Corros Sci. 2018;135:197–206.
47. Magar HS, Hassan RYA, Mulchandani A. Electrochemical impedance spectroscopy (EIS): principles, construction, and biosensing applications. Sensors. 2021;21:6578.
48. Fadl-Allah SA, Mohsen Q. Characterization of native and anodic oxide films formed on commercial pure titanium using electrochemical properties and morphology techniques. Appl Surf Sci. 2010;256:5849–55.
49. Ahmadi S, Mohammadi I, Sadrnezhaad SK. Hydroxyapatite based and anodic Titania nanotube biocomposite coatings: fabrication, characterization and electrochemical behavior. Surf Coat Technol. 2016;287:67–75.
50. Cui ZD, Zhu JM, Jiang H, Wu SL, Zhu SL. Research progress of the surface modification of titanium and titanium alloys for biomedical application. Acta Metall Sin. 2022;58:837–56.
51. Zhao XT, Hu JL, Nie JJ, Chen DF, Qin GW, Zhang ER. Enhanced antibacterial activity, corrosion resistance and endothelialization potential of Ti-5Cu alloy by oxygen and nitrogen plasma-based surface modification. J Mater Sci Technol. 2024;168:250–64.
52. Ye J, Li B, Li M, Zheng YF, Wu SL, Han Y. Formation of a ZnO nanorods-patterned coating with strong bactericidal capability and quantitative evaluation of the contribution of nanorods-derived puncture and ROS-derived killing. Bioact Mater. 2022;11:181–91.
53. Majidi RF, Mesgar ASM, Milan PB. Surface-modified, zinc-incorporated mesoporous silica nanoparticles with improved antibacterial and rapid hemostatic properties. Colloids Surf B. 2024;243:114132.
54. Koons GL, Diba M, Mikos AG. Materials design for bone-tissue engineering. Nat Rev Mater. 2020;5:584–603.
55. Manwaring ME, Walsh JF, Tresco PA. Contact guidance induced organization of extracellular matrix. Biomaterials. 2004;25:3631–8.
56. Lei H, Yi T, Fan H, Pei X, Wu L, Xing F, Li M, Liu L, Zhou C, Fan Y, Zhang X. Customized additive manufacturing of porous Ti6Al4V scaffold with micro-topological structures to regulate cell behavior in bone tissue engineering. Mater Sci Eng C. 2021;120:111789.
57. Hou Y, Xie W, Yu L, Camacho LC, Nie C, Zhang M, Haag R, Wei Q. Surface roughness gradients reveal Topography-Specific mechanosensitive responses in human mesenchymal stem cells. Small. 2020;16:e1905422.
58. Kang AR, Oh YR, Kim HY, Park MJ, Joo BS, Choi WJ, Lee JY, Jung MH, Ji YI, Choi JS. Up-regulation of inhibitors of DNA binding/differentiation gene during alendronate-induced osteoblast differentiation. Arch Gynecol Obstet. 2012;285:1331–8.
59. Komori T. Runx2, an inducer of osteoblast and chondrocyte differentiation. Histochem Cell Biol. 2018;149:313–23.
60. Cai HX, Wang PL, Xu Y, Yao Y, Liu J, Li T, Sun Y, Liang J, Fan YJ, Zhang XD. BMSCs-assisted injectable col I hydrogel-regenerated cartilage defect by reconstructing superficial and calcified cartilage. Regener Biomater. 2020;7:35–46.
61. Komori T. Functions of osteocalcin in bone, pancreas, testis, and muscle. Int J Mol Sci. 2020;21:7513.
62. Tao BL, Yi WW, Qin X, Wu JJ, Li K, Guo A, Hao J, Chen LX. Improvement of antibacterial, anti-inflammatory, and osteogenic properties of OGP loaded Co-MOF coating on titanium implants for advanced osseointegration. J Mater Sci Technol. 2023;146:131–44.
63. Hou Y, Yu LX, Xie WY, Camacho LC, Zhang M, Chu ZQ, Wei Q, Haag R. Surface roughness and substrate stiffness synergize to drive cellular mechanoresponse. Nano Lett. 2020;20:748–57.
64. Sikavitsas VI, Temenoff JS, Mikos AG. Biomaterials and bone mechanotransduction. Biomaterials. 2001;22:2581–93.
65. Shiu HT, Goss B, Lutton C, Crawford R, Xiao Y. Formation of blood clot on biomaterial implants influences bone healing, tissue eng. Part B. 2014;20:697–712.
66. Hamlet SM, Lee RSB, Moon HJ, Alfarsi MA, Ivanovski S. Hydrophilic titanium surface-induced macrophage modulation promotes pro-osteogenic signalling. Clin Oral Implants Res. 2019;30:1085–96.
67. Park JW, Kim YJ, Jang JH, Kwon TG, Bae YC, Suh JY. Effects of phosphoric acid treatment of titanium surfaces on surface properties, osteoblast response and removal of torque forces. Acta Biomater. 2010;6:1661–70.

Publisher's note